Fall 12-15-2023

Effects of Back Reflectors and Thin Metal Covers on the Performance of Near-field Thermophotovoltaic Devices

Mehran Habibzadeh
University of Maine, mehran.habibzadeh@maine.edu

Recommended Citation

Habibzadeh, Mehran, "Effects of Back Reflectors and Thin Metal Covers on the Performance of Near-field Thermophotovoltaic Devices" (2023). *Electronic Theses and Dissertations*. 3898.
https://digitalcommons.library.umaine.edu/etd/3898

EFFECTS OF BACK REFLECTORS AND THIN METAL COVERS ON THE PERFORMANCE OF NEAR-FIELD THERMOPHOTOVOLTAIC DEVICES

By

Mehran Habibzadeh

B.S. K. N. Toosi University of Technology, 2020

A THESIS
Submitted in Partial Fulfillment of the
Requirements for the Degree of
Master of Science
(In Mechanical Engineering)

The Graduate School
The University of Maine
December 2023

Advisory Committee:

Sheila Edalatpour, Associate Professor of Mechanical Engineering, University of Maine, Advisor
Bashir Khoda, Associate Professor of Mechanical Engineering, University of Maine
Olivier Putzeys, Senior Lecturer of Mechanical Engineering, University of Maine

EFFECTS OF BACK REFLECTORS AND THIN METAL COVERS ON THE PERFORMANCE OF NEAR-FIELD THERMOPHOTOVOLTAIC DEVICES

By Mehran Habibzadeh

Dissertation Advisor: Dr. Sheila Edalatpour

An Abstract of the Thesis Presented
in Partial Fulfillment of the
Requirements for the Degree of
Master of Science
(In Mechanical Engineering)
December 2023

Highly efficient energy harvesting devices that can recover a large amount of waste energy are of significant interest. Thermophotovoltaics (TPVs) are solid-state devices that can convert thermal energy radiated by a heated emitter into electrical power through the process of photovoltaic effect. In a TPV system, heat is converted to electricity by using a high-temperature emitter to radiate photons, which are then absorbed by a photovoltaic (PV) cell, generating electron-hole pairs and producing electrical power.

TPV devices have the advantages of producing High efficiency and being lightweight with low maintenance cost and zero pollution. However, these devices have not been commercialized yet as their power output is low. A promising mechanism for increasing the power output and also the efficiency of the TPV cells is by reducing the gap distance between the emitter and the PV cell of the device to a value that is smaller than the dominant wavelength of thermal radiation (~ 10 mm at room temperature). In this case, thermally radiated evanescent electromagnetic waves,

which are only substantial at sub-wavelength distances from the emitter, can also be received by PV cells and contribute to power generation. These devices with a sub-wavelength separation gap between the emitting layer and the received are referred to as near-field thermophotovoltaic (NF-TPV) devices.

It has been proposed that using a reflector at the back side of the PV cell, introducing a thin metal cover on the PV cell, and creating an air gap between the PV cell and the back reflector can increase the power output and/or the efficiency of the NF-TPV devices. However, it is not known how the performance of the NF-TPV devices changes with using air gap and thin metal layer simultaneously.

This thesis examines the effect of the air gap and the presence of the metal cover layer of the NF-TPV devices for a vacuum gap size of 50 nm between the emitter and the PV cell. Also, a new configuration where both the air gap and the metal cover have been used simultaneously, is proposed. Finally, by using genetic algorithms, novel NF-TPV devices with high efficiency and power output are designed. Based on the results, it is seen that utilizing the air gap increases the efficiency of a NF-TV device having a vacuum gap of 50 nm by 10%. However, the power output of the device decreases in the presence of the air gap due to a reduction in the in-band radiation absorption by the PV cell. The air gap is more beneficial at small vacuum gap sizes, such as 10 nm, where both the power output and the efficiency increase with introducing an air gap. It also is shown that, for a NF-TPV device with a vacuum gap size of 50 nm, depositing a very thin metal layer, around 3 nm, on top of the PV cell increases the power output of the NF-TPV nearly by a factor of 4. In this case, efficiency decreases from 30% to 20%. Therefore, placing a thin metal layer on top of the PV cell is practical for waste heat recovery applications where power output is more important than efficiency.

The results of this thesis can provide a guide for designing high-power output and large-efficiency NF-TPV devices that can be used for converting heat from any source, including waste heat, to useful electrical power.

ACKNOWLEDGEMENTS

I express my heartfelt thanks to my advisor, Dr. Sheila Edalatpour, for her steadfast support and invaluable guidance throughout my two-year journey towards obtaining my master’s degree. Her expertise, dedication, and constructive feedback have been instrumental in shaping the trajectory of my research and academic pursuits. I am profoundly thankful for her mentorship, patience, and encouragement, which have not only enriched my academic experience but also played a pivotal role in my personal and professional growth. Her commitment to excellence and passion for knowledge have been a constant source of inspiration, and I am truly fortunate to have had the privilege of working under her guidance. My Master's journey has been immensely rewarding, thanks to her mentorship and support.

I want to thank Dr. Bashir Khoda and Dr. Olivier Putzeys who agreed to be my committee members. Also, I would like to express my thanks to my colleagues in the laboratory, Saman Zare, Ramin Pourya, Md. Shofiqul Islam, and Md. Jahid Hasan Sagor for all their helps and supports.

Finally, I want to express my sincere gratitude to my parents, Mohsen and Frangis, and my sister, Mahsa, for their unwavering support. Their contributions were indispensable to my success on this journey. At the end, I want to say thank you to my beloved wife, Yasaman, for being my rock, source of endless encouragement, and the pillar of strength that made this academic endeavor not only possible but also immensely rewarding.

TABLE OF CONTENTS

LIST OF FIGURES

CHAPTER 1

INTRODUCTION

1.1. Personal Motivation

All the choices we make today, can influence the future, and make it better or worse. I have made a choice to do research in the field of energy and study sustainable sources of energies, due to the fact that we need replacements for the conventional source of energies like fossil fuels that cause harmful effects on the environment. By employing efficient sustainable sources of energy, we can minimize the harmful effects on nature and make Earth a better place for the next generations. As a Mechanical engineer, I have devoted the last 2 years of my life, my master's program, and much more time in the future to development in the field of renewable energies. Specifically, I have been working on developing Thermophotovoltaic (TPV) devices as I believe that they can play a significant role in saving energy. The reasons that I believe TPV systems can be categorized as green technologies and be considered sustainable are as below:

- **Use of renewable heat sources**: They can be powered by renewable energy sources like solar energy or even geothermal heat.
- **Waste heat recovery**: TPV systems can be applied to capture and convert the generated waste heat by industrial processes which cause harmful effects like global warming by being released into the environment.
- **Low environmental impact**: TPV devices cause low environmental impacts, as they do not generate greenhouse gases during operation.

From my perspective, the development of TPV systems can save a great deal of energy for us and make the world better and safer for the next generations. I hope that my contributions play a modest role in advancing TPV technology, thereby contributing to the enhancement of efficiency in TPV systems.

1.2. Thermal Radiation and Its Regimes

Any material with a temperature above absolute zero emits thermal radiation in the form of electromagnetic waves. This thermal radiation arises from the random movements of charged particles within the material. When the distance from the emitting object exceeds the associated thermal wavelength, $\lambda_{\max}$, the emission of thermal waves is categorized as far-field thermal radiation. The value of $\lambda_{\max}$, typically around 10 μm under standard conditions like room temperature, can be calculated using Wien's displacement law as follows [1]:

$$\lambda_{\max}T = 2898\ \mu\mathrm{m.K} \tag{1.1}$$

Here, T denotes the temperature of the emitting medium. Planck's theory is employed to elucidate the characteristics of thermal radiation in the far-field regime [2-3]. According to Planck's theory, far-field thermal radiation is confined to the radiation emanating from an ideal emitter, recognized as a blackbody. Planck's theory solely considers the involvement of propagating waves, characterized by a parallel component of the wavevector, k_ρ, smaller than that for free space, k_0. The term "far-field" for these electromagnetic waves implies that they can propagate over significant distances relative to the surface of the emitting medium. Additionally, Planck's theory does not account for wave interference. Waves thermally emitted at distances approximately equal to or smaller than $\lambda_{\max}$ from the emitting subject are termed near-field thermal radiation. In the near-field regime, the predominant portion of thermal radiation consists of evanescent waves, which decay exponentially over a distance roughly equivalent to $\lambda_{\max}$ from the surface of the emitting medium (refer to Fig. 1.1). The contribution of evanescent waves results in near-field thermal radiation being orders of magnitude higher than far-field thermal radiation [4].

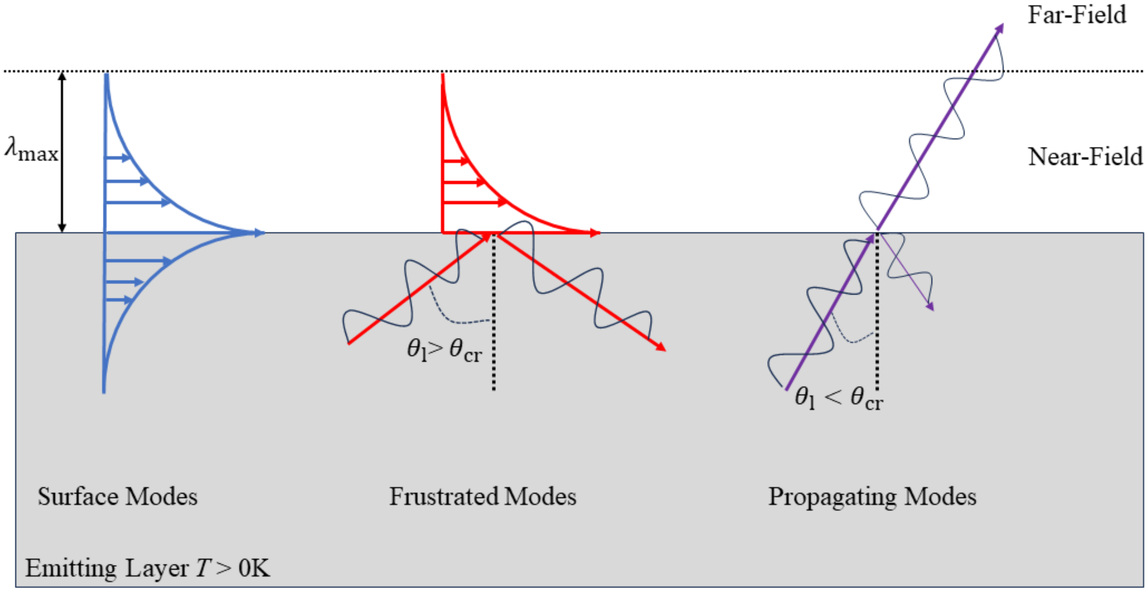

Fig. 1.1 Different modes of thermal radiation, surface, frustrated and propagating modes

The evanescent waves can encompass frustrated or surface modes which are depicted in Fig. 1.1 for an emitter, emitting waves to free space medium. The frustrated modes are evanescent in the free space medium but propagate inside the emitting medium. It means that they have $k_0 < k_\rho < n_{\text{emit}} k_0$ where n_{emit} is the emitting medium's refractive index. These waves arrive at the interface between the emitter layer and vacuum space with an incident angle (θ_I) that exceeds the critical angle $\theta_{cr} = 1/\sin^{-1} n_E$. Consequently, they undergo total internal reflection at the interface between free space and the emitting layer, and they exist as evanescent waves within the free space region. Frustrated modes make broadband enhancement in the near-field thermal radiation. Regarding surface modes, they are evanescent in both mediums, emitting and free space, as their k_ρ values are higher than that of both media, $k_0 < k_\rho$ and $k_\rho > n_{\text{emit}} k_0$. In metallic materials, doped semiconductors, and polar dielectrics, the oscillations of free electrons give rise to an augmentation in the thermal emission of surface modes known as surface plasmon polaritons (SPPs) and surface phonon polaritons (SPhPs), respectively. The thermal emission associated with SPPs and SPhPs results in a quasi-monochromatic enhancement in near-field thermal radiation [5].

1.3.Thermal Radiation in Near-Field Regime

Fluctuational electrodynamics is used to investigate the behavior of the near-field thermal radiation [6]. In fluctuational electrodynamics, a term referring to stochastic current density, $\mathbf{J}^{fl}$, is introduced to the Maxwell equations to consider the stochastic, heat-induced movements of the charged particles in a non-magnetic emitter [7]:

$$\nabla \times \mathbf{E}(\mathbf{r}, \omega) = \mathrm{i}\omega\mu_0 \mathbf{H}(\mathbf{r}, \omega) \tag{1.2}$$

$$\nabla \times \mathbf{H}(\mathbf{r}, \omega) = -\mathrm{i}\omega\varepsilon \mathbf{E}(\mathbf{r}, \omega) + \mathbf{J}^{fl}(\mathbf{r}, \omega) \tag{1.3}$$

$$\nabla \times \mathbf{E}(\mathbf{r}, \omega) = 0 \tag{1.4}$$

$$\nabla \times \mathbf{H}(\mathbf{r}, \omega) = 0 \tag{1.5}$$

Where ω, μ_0 and ε refer to the angular frequency, free space medium's permeability and permittivity of the emitting medium, respectively. **E** and **H** stand for electric and magnetic fields measured at position **r** in the space, correspondingly. The first moment of $\mathbf{J}^{fl}$, the ensemble average**,** is zero for a non-magnetic media. The relation between the second moment of $\mathbf{J}^{fl}$, the ensemble average of spatial correlation function, with the material properties like emitter's temperature is captured utilizing fluctuation-dissipation theorem as flows [6]:

$$\left\langle J_{\alpha}^{fl}(\mathbf{r}, \omega) J_{\beta}^{fl\dagger}(\mathbf{r}', \omega) \right\rangle = \frac{4}{\pi}\omega\varepsilon_0 \mathrm{Im}[\varepsilon]\Theta(\omega, T)\delta(\mathbf{r} - \mathbf{r}')\delta_{\alpha\beta} \tag{1.6}$$

Where ε_0, Θ and T are the free space permeability, the mean energy of an electromagnetic state and temperature of the media, respectively. Superscripts, α and β are perpendicular components and † stands for the Hermitian operator. Finally, $\delta_{\alpha\beta}$ and $\delta(\mathrm{r} - \mathrm{r}')$ are Kronecker delta and Dirac delta function, correspondingly. **E** and **H** are found by solving Eqs. 1.2 to 1.4 [7] and the spectral energy density, u, at point **r** in the space can be calculated using **E** and **H** values as follows [8]:

$$u(\mathbf{r}, \omega) = \frac{1}{4}\varepsilon_0 \mathrm{Trace}\langle \mathbf{E}(\mathbf{r}, \omega) \otimes \mathbf{E}(\mathbf{r}, \omega)\rangle + \frac{1}{4}\mu_0 \mathrm{Trace}\langle \mathbf{H}(\mathbf{r}, \omega) \otimes \mathbf{H}(\mathbf{r}, \omega)\rangle \tag{1.7}$$

Where ⊗ is used to show the outer product. The values of **E** and **H** for simple configurations like planar medias, can be obtained analytically utilizing the dyadic Green's functions, whereas numerical simulations are needed for more complicated configurations. **E** and **H** can be calculated with using dyadic Green's functions as follows [7]:

$$\mathbf{E}(\mathbf{r},\omega) = \mathrm{i}\omega\mu_0 \int_V \bar{\bar{G}}^E\,(\mathbf{r},\mathbf{r}',\omega)\,.\,\mathbf{J}^{fl}(\mathbf{r}',\omega)dV' \tag{1.8}$$

$$\mathbf{H}(\mathbf{r},\omega) = \int_V \bar{\bar{G}}^H\,(\mathbf{r},\mathbf{r}',\omega)\,.\,\mathbf{J}^{fl}(\mathbf{r}',\omega)dV' \tag{1.9}$$

By plugging Eqs. (1.6), (1.8) and (1.9) into Eq. (1.7), the spectral energy density at point $\mathbf{r}$ in the space caused by radiation of an emitter can be found as:

$$u(\mathbf{r},\omega) = \frac{k_0^2}{\pi\omega}\mathrm{Im}[\varepsilon]\Theta(\omega,T)\int_V \mathrm{Trace}\left[k_0^2\bar{\bar{G}}^E(\mathbf{r},\mathbf{r}').\,\bar{\bar{G}}^{E\dagger}(\mathbf{r},\mathbf{r}') + \bar{\bar{G}}^H(\mathbf{r},\mathbf{r}').\,\bar{\bar{G}}^{H\dagger}(\mathbf{r},\mathbf{r}')\right]dV' \tag{1.10}$$

Pointing vector, **S**, can be used to calculate the radiated heat transfer from one media to another separated by a near-field distance. The time-averaged Pointing vector can be written as:

$$\langle\mathbf{S}(\mathbf{r},\omega)\rangle = \frac{1}{2}\mathrm{Re}\big[\langle\mathbf{E}(\mathbf{r},\omega)\times\mathbf{H}^\dagger(\mathbf{r},\omega)\rangle\big] \tag{1.11}$$

With plugging Eqs. (1.6), (1.8) and (1.9) in Eq. (1.11) the time-averaged pointing vector can be calculated as:

$$\langle\mathbf{S}(\mathbf{r},\omega)\rangle = \frac{2}{\pi}k_0^2\,\mathrm{Im}[\varepsilon]\Theta(\omega,T)\mathrm{Re}[\mathrm{i}\int_V G^E_{m\alpha}(\mathbf{r},\mathbf{r}',\omega)G^{H\dagger}_{n\beta}(\mathbf{r},\mathbf{r}',\omega)dV'] \tag{1.12}$$

Where the subscripts m and n show the perpendicular components and k_0 stands for the wavevector in the free space medium. With having the dyadic Green's functions Eq. (1.12) can be used to find the radiative heat flux between to mediums.

1.4. Applications of Near-Field Radiative Heat Transfer

Near-field radiative heat transfer has attracted significant attention owing to its diverse potential applications. These applications encompass near-field thermophotovoltaic (TPV) cells [9-26], heat management in electronic devices [27-29], thermal rectification [30-44], and imaging [45-46]. In TPV devices by reducing the gap distance between the emitting layer and the PV cell, the power density of the TPV cell undergoes a substantial increase, primarily attributable to the contribution of evanescent waves. [9-26]. Near-field thermal radiation introduces a contactless approach that enables heat dissipation from specific high temperature regions within micro- and nanostructures which can be utilized for radiative cooling of the electronic components [27-29]. An additional promising area of using near-field thermal radiation lies in thermal rectifiers. These devices introduce a temperature-dependent directionality in radiative heat transfer between two medias, exhibiting potential applications in managing heat flow [30-44]. The mentioned near-field rectifiers operate based on the changes in the dielectric constants of the two materials in response to temperature fluctuations. This temperature-induced variations in dielectric constants leads to a shift in the resonance frequencies of near-field thermal radiation for each material. Consequently, a reversal in temperature difference, causes an asymmetry in radiative heat flux between the two medias to be generated. Furthermore, near-field thermal radiation provides application in thermal radiation scanning tunneling microscopy (TRSTM), enabling advanced high-resolution imaging [45-46]. Within the TRSTM approach, the evanescent waves generated by a heated sample are redirected to the distant field by a finely pointed atomic force microscope (AFM) tip, located at proximity to the sample. These redirected fields give insights into the localized characteristics of the sample's material and structure. This technique gives opportunity of thermal imaging from nanostructured surfaces without needing external illumination.

1.5. Thermophotovoltaic Devices Importance and Related Literatures

In American industries, roughly 20-50% of the energy is wasted and discharged into the surroundings in different forms of hot exhaust gases, heat lost from high-temperature surfaces, and cooling water [47]. As an example, in transportation, about 20% of the consumed fuel is used for functional purposes like generating forward motion; while the remained energy is wasted as exhaust gases or channeled into a cooling system which lonely accounts for 36% of the entire wasted energy in the United States [48]. Consequently, capturing this massive amount of energy is crucial to make enhancement of energy utilization efficiency and curb carbon emissions. Currently, the predominant applied methodology for energy harvesting purposes is thermoelectric generators (TEG) which can deliver an approximate power density of 1 W/cm^2 when being in contact with the intermediate temperature sources (~ 500–900 K) with efficiencies moderately limited at around (<10%) [49]. Improving their efficiencies to a greater extent needs developing novel thermoelectric materials characterized by high figures of merits, which is presently a dynamic area in the research [50-51].

Thermophotovoltaics (TPVs) are accounted as an attractive alternate solid-state strategy for recuperating waste heat [52]. TPV generators are able to directly transform thermal energy emitted by a heated emitter into electrical energy through the process of photovoltaic effect. The phenomenon of photovoltaic effect was first introduced by E. Becquerel in 1839 through the utilization of an electrochemical cell [53]. Conversion of light to electricity is recognized as photovoltaic effect. Diverse heat sources including industrial waste heat and concentrated solar panels have the capacity to provide the energy needed to elevate the emitter's temperature [54-56]. As far-field thermal radiation is inherently constrained in its power density by the blackbody limit, substantial theoretical [57-63] and experimental [64] endeavors have been investigating the near-field TPV systems. In these setups, by decreasing the separation gap between the PV cell and the emitting layer to a scale smaller than the corresponding thermal wavelength, the power density can surpass what is achievable in the far-field configurations. There has been an active research about near-field thermophotovoltaics (NF-TPV) devices over the past years after being introduced by numerous studies in the early 2000s [65-66]. It has been demonstrated that reducing the separation gap distance between the emitter and the PV cell leads to a boost in photogeneration by several orders of magnitude [67-69]. Benefitting from these advantages, NF-TPV configurations can attain elevated levels of both conversion efficiency and substantial power output density which are not accessible in the far-field cases. In Fig 1.2(a) the maximum power output and the efficiency of the TPV structure shown in Fig 1.2(b) is presented. The distance between the emitter and the PV cell, d, is reduced to the nanometer scale. The thermally emitted evanescent waves (which are only substantial at nanometer scale distances from the emitter surface) can enhance the power output of the NF-TPV devices by orders of magnitude compared to the conventional TPVs (enhancement of 10 times for d = 100 nm and 232 times for d = 10 nm). So, to gain high values for both power output and efficiency it is necessary to use NF-TPV configurations. The mechanism of the TPV devices is explained in detail in the subsequent chapters.

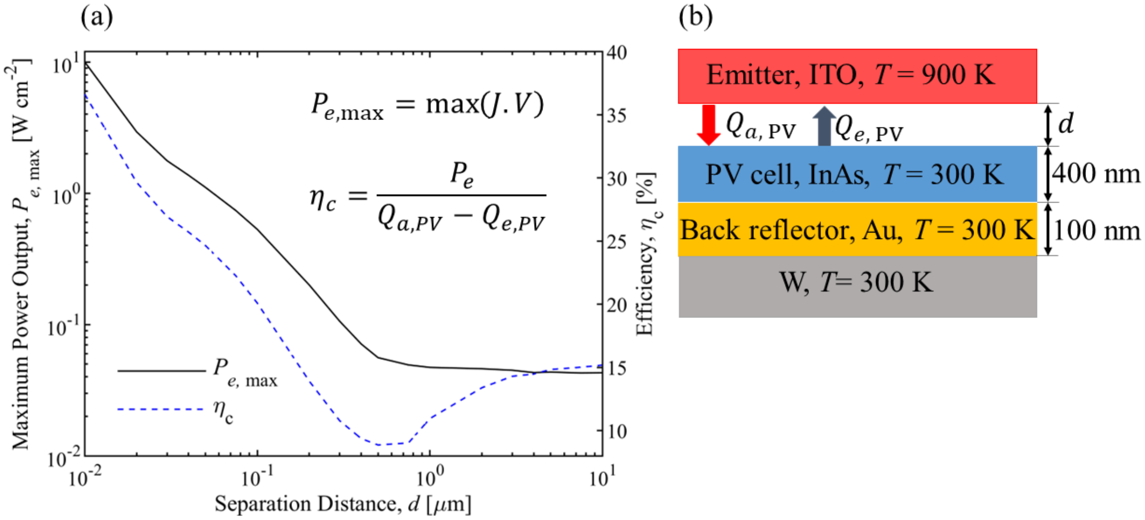

Fig. 1.2 (a) The maximum power output and efficiency of a NF-TPV device versus the separation distance of the emitter and the PV cell, d. (b) The schematic of the under-study TPV device with high temperature and low temperature of 900 K and 300 K, respectively.

1.6. The Main Goals and Outline of The Thesis

The main goal of this study is to investigate different methods for enhancing the performance, efficiency and power output, of the Near-Field TPV devices. The next chapter, chapter 2, and its subsections are dedicated to explaining the mechanism of the Near-field TPV device and also reviewing different ways to improve the overall performance of the TPV device. In chapter 3 two different ways to increase the efficiency and power output of the TPV devices are thoroughly investigated and TPV configurations exhibiting high power output and efficiency values are designed with using Genetic algorithm.

CHAPTER 2

COMPREHENSIVE EXPLANATION OF NEAR-FIELD THERMOPHOTOVOLTAIC DEVICE AND ITS MECHANISM

2.1. Understanding Thermophotovoltaic (TPV) Devices: Components, Mechanism, and Operational Principles

2.1.1. TPV Mechanisms and Important Performance Metrices

A TPV device has two main parts; an emitting layer and a PV cell as presented in Fig. 2.1(a). The PV cell is made of a material that has a band gap. When the emitted photons by thermal emitter with energy levels higher than the band gap are absorbed by the PV cell, electron-hole pairs (EHPs) are formed due to photovoltaic effect. Conversely, when EHPs within the PV cell recombine, they generate photons with energy levels surpassing the bandgap energy. This phenomenon is recognized as radiative recombination. The emitted radiation (Q_e) from the PV cell, specifically the spectral radiation above the bandgap, is predominantly a result of radiative recombination. Once the formed EHPs go through the electrodes, they result in generation of photocurrent inside the external circuit. However, not all the generated EHPs can reach the electrodes and lead to current production. Some of them are lost, recombined, through different mechanisms, including non-radiative, radiative, and surface recombination. Internal quantum efficiency is the ratio of the number of EHPs that have contribution to photocurrent generation to the number of absorbed photons by the PV cell. There are two other metrices that are important to judge the performance of the TPV cells: First, the power conversion efficiency, η_c, and second, power output, P_e, of the TPV cell. The formulas to calculate them are shown in the inset of the Fig.2.1(b) and they will be explained completely in the following sections. The variation of the generated photocurrent versus the voltage of the PV cell (i.e., J-V characteristics) is shown in Fig. 2.1(b). Two parameters J_{sc} and V_{oc} refer to the short circuit current (i.e., measured current when $V = 0$) and open circuit voltage (i.e., measured voltage when $J = 0$), respectively. As it is shown in Fig.2.1(b), by applying V to the cell, the photocurrent decreases. The reason of this behavior is formation of dark current, generating via diffusion and recombination of charge carriers moving in the counter direction of the photocurrent. The operating voltage range of the PV cell is $0 < V < V_{oc}$. The highest value of the product of J and V, in the interval of $[0\ V_{\mathrm{oc}}]$, refers to maximum electrical power output P_e. The

Power conversion efficiency η_c of the TPV cell is defined as the ratio of P_e to the total radiative heat flux $(Q_a - Q_e)$, where Q_a stands for the radiative heat transfer from emitter toward the PV cell.

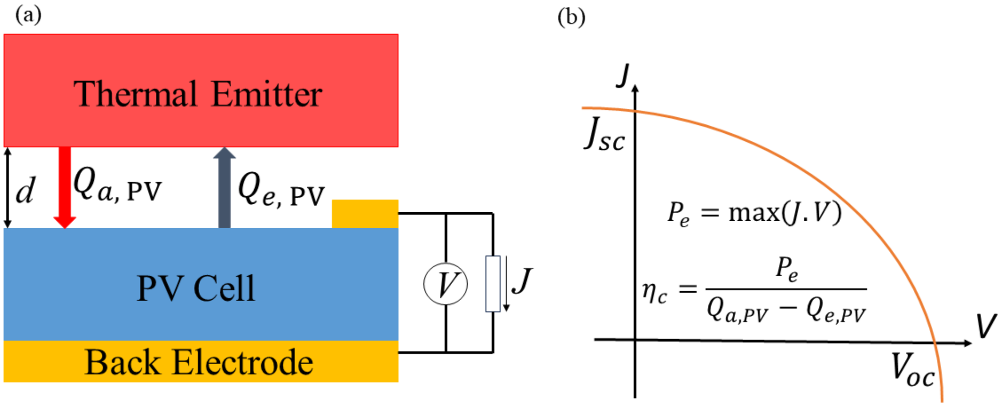

Fig. 2.1 (a) The schematic of the TPV device. (b) The *J-V* characteristic of the TPV device.

2.1.2. Different TPV Loss Terms and Possible Solutions To Minimize Them

As it was mentioned earlier not all the absorbed radiative heat fluxes by the PV cell, can contribute to P_e. The losses can be classified as radiative, electrical, and thermal (see Fig. 2.2) [70]. Radiative losses which are also known as parasitic absorption losses, pertain to radiative energy absorbing by lattice structure and free moving carriers of the PV cell that do not have any contribution to photocurrent generation. These losses are mainly made of out-of-band (i.e., photons with energy levels lower than the band gap of the cell) photon absorption by the cell. A common approach to mitigate radiative losses is employing a thin PV cell and make use of a backside electrode as a reflector which helps in redirecting sub-bandgap radiation back towards the emitter [71-74]. Electrical losses which are known as photocurrent losses are resulting from surface and bulk (radiative and non-radiative) recombination. Non-radiative recombination includes Auger, Shockley-Read-Hall (SRH) and surface recombination which are explained in the following sub-sections and Fig. 2.3 represents them. Electrical losses decrease the functional EHPs leading to reduction in power output of the cell.

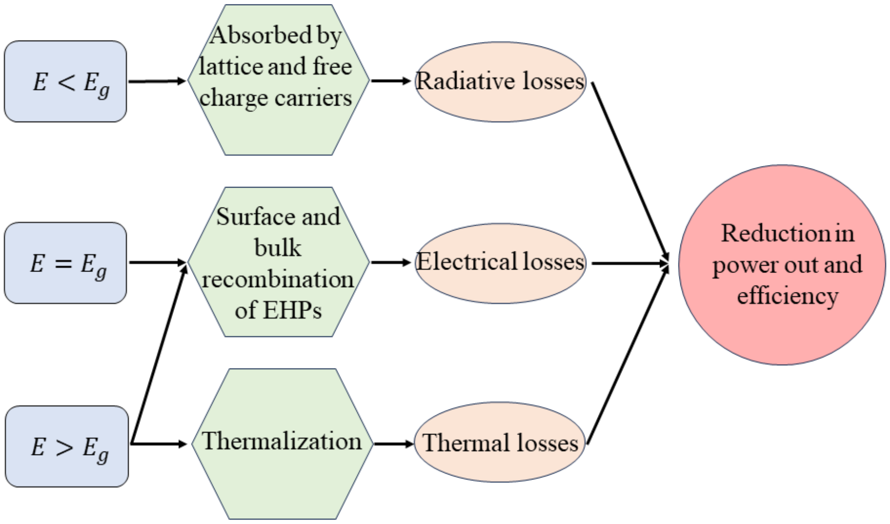

Fig. 2.2 Different loss terms, Radiative, Electrical and Thermal, and their effects on the performance of the TPV device.

One effective approach to reduce the electrical losses is utilizing thin PV cells [49,73-75]] as the rate of bulk recombination decreases with the PV cell's thickness. Thermal losses arise when the surplus radiative energy, which consists of photons with energy levels higher than the bandgap and is not utilized for generating EHPs, gets converted into thermal energy within the PV cell. One common way to curb thermal losses is to set the temperature of the emitter at which the spectral radiative heat flux's peak aligns closely with the bandgap [76]. Furthermore, applying tandem PV cells (i.e., arranging PV cells in a series from low to high band gap energies) offers the opportunity to design each sub cell in a way that it absorbs radiative energy near its specific bandgap energy [77].

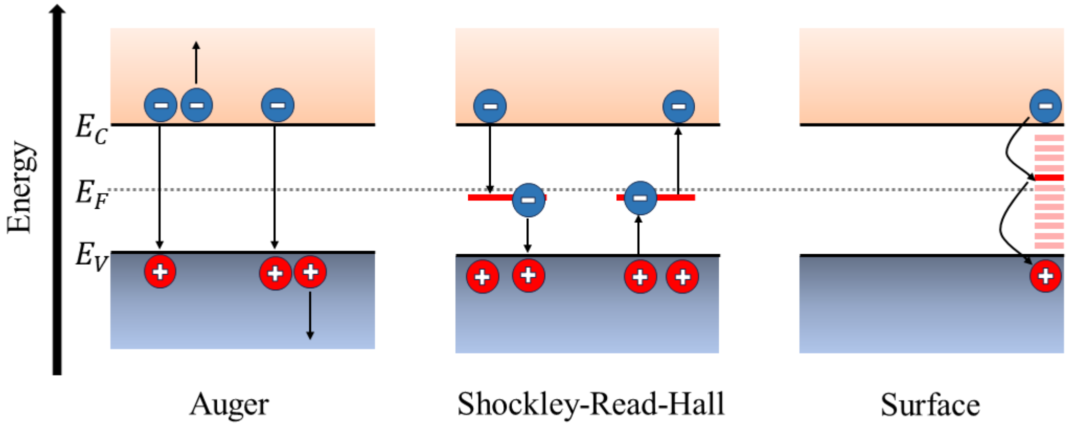

Fig. 2.3 The schematic of three different non-radiative losses, Auger, Shockley-Read-Hall, and Surface recombination.

2.1.2.1. Auger Recombination

A physical phenomenon referred to as the impact ionization effect occurs when a high-energy electron collides with an atom, transferring sufficient energy to an electron from the atom's structure, and as a result forming an electron-hole pair. Auger effect represents the inverse mechanism of this process [78]. In Auger recombination the released energy by recombination of a hole and an electron is passed to another electron, in valence or conduction band) rather than emitting the excess energy as a photon. The new exited electron loses its excess energy through a sequence of collisions with the lattice and then relaxing at the edge of the band [79]. As this process relies on the capacity of charge carriers to transfer energy, the probability of Auger recombination goes up with having higher concentration of charge carriers. The Auger recombination rate can be determined as [80]:

$$R_{\text{Auger}} = (C_e n + C_h p)(np - {n_i}^2)t \tag{2.1}$$

Where, n and p are, respectively, electron and hole concentrations, n_i refers to the intrinsic carrier concentration, t is the PV cell's thickness, and $C_{(e,h)}$ is the Auger recombination coefficients for electron and holes.

2.1.2.2. Shockley-Read-Hall (SRH) Recombination

The lifetime of the charge carriers is influenced by the impurities and defects existed in the semiconductor's crystal. A modified electronic structure can cause the energy levels of the defects to raise and do not lie close to the edge of the bands. These impurity levels that might lie within the forbidden band are referred to trap levels because the play as a trap for charge carriers [78]. The SRH recombination rate can be calculated as follows [73]:

$$R_{\mathrm{SRH}} = \frac{(np - {n_i}^2)t}{\tau_{\mathrm{SRH},h}\left(n + n_{t,b}\right) + \tau_{\mathrm{SRH},e}\left(p + p_{t,b}\right)} \tag{2.2}$$

Where, $n_{t,b}$ and $p_{t,b}$ are, respectively, the electron and hole trap concentrations, which are typically considered to be equal to n_i [81]. $\tau_{\mathrm{SRH},h}$ and $\tau_{\mathrm{SRH},e}$ are bulk SRH lifetimes for holes and electrons, respectively. The simplified version of R_{SRH} by considering that $n_{t,b} = p_{t,b} = n_i$ and $\tau_{\mathrm{SRH},h} = \tau_{\mathrm{SRH},e} = \tau$ can be written as:

$$R_{\mathrm{SRH}} = \frac{(np - {n_i}^2)t}{\tau(n + p + 2n_i)} \tag{2.3}$$

2.1.2.3. Surface Recombination

The recombination that happens at the semiconductor's surface is termed as surface recombination. This happens when traps are formed at or close to the surface of the semiconductor or interface dues to unpaired bonds caused by presence of discontinuation in the crystal. Surface recombination depends on the surface recombination velocity which is influenced by the defect's concentration on the surface [82]. The equation used to calculate surface recombination rate is as follows [82]:

$$R_{\mathrm{surf},(n,p)} = \frac{np - {n_i}^2}{\dfrac{n + n_{t,s}}{S_{h,(n,p)}} + \dfrac{p + p_{t,s}}{S_{e,(n,p)}}} \tag{2.4}$$

Where, $R_{\mathrm{surf},(n,p)}$ stands for the surface recombination rate for *n*- and *p*-doped side; The total surface recombination rate is sum of n- and p-doped recombination (i.e., $R_{\mathrm{surf}} = R_{\mathrm{surf},n} + R_{\mathrm{surf},p}$). $S_{e,(n,p)}$ and $S_{h,(n,p)}$ represent the electron and hole recombination velocities on the n- and p-doped sides, respectively. $n_{t,s}$ and $p_{t,s}$ stand for electron and hole surface trap concentrations which commonly considered to be equivalent to n_i [81].

2.1.3. Near Field Thermal Radiation in a 1D Layered TPV Device

Fig. 2.4 represents a schematic of a 1-D layered TPV cell utilized in this subsection. As Fig. 2.4 shows the TPV cell is composed of $m+1$ layers; Mediums 0 and 1 correspond to emitter and vacuum, respectively. The PV cell is made of layers 2 to m. Subscript 's' indicated the emitter, and subscript 'c' indicates the PV cell, and subscript 'j' indicated the jth layer of the PV cell. Therefore, any layer l within the TPV device will be assigned a value ranging from 0 to m, while any layer j within the PV cell will have a value ranging from 2 to m. T_c and T_s ,respectively, refer to PV cell and emitter temperatures. The temperature across the PV cell is considered to be consistent, and $T_c = T_j$.

A general formula to find the flux emitted by layer l and subsequently absorbed by layer j is as follow [81,83-84]:

$$\phi_{sj}(\omega) = \left(\frac{k_0}{\pi}\right)^2 Re\left[i\mathrm{Im}(\varepsilon_l)\int_0^\infty k_\rho\, dk_\rho \times \int_{z_{l-1}}^{z_l}\{F(\omega,k_\rho,z,z_{j-1}) - F(\omega,k_\rho,z,z_j)\}dz\right] \quad (2.5)$$

Where, k_0 and k_ρ are the wavevector of the free space and wavevector parallel to the surface ($k_0 = \frac{\omega}{c}$) with c being the speed of the light. ε_l stands for the refractive index of the layer l. The function $F(\omega, k_\rho, z, z_j)$ can be obtained by having the Weyl components of the dyadic Green's tensors. The frequency and temperature dependent mean energy of Planck oscillator can be found using equation below [85-86]:

$$\Theta(\omega, T) = \hbar\omega\psi(\omega, T) \quad (2.6)$$

Where the modified Bose-Einstein distribution can be found as [81,86]:

$$\psi(\omega,T,\mu) = \begin{cases} \dfrac{1}{\exp\left(\dfrac{\hbar\omega-\mu}{k_B T}\right)-1} & (\hbar\omega \geq E_g) \\ \dfrac{1}{\exp\left(\dfrac{\hbar\omega}{k_B T}\right)-1} & (\hbar\omega < E_g) \end{cases} \quad (2.7)$$

Where k_B and $\hbar$ are, respectively, Boltzmann and reduced Planck constants and E_g stands for the band gap energy level. The photon chemical potential μ can be defined as the difference between the electron and hole quasi-Fermi energy levels [86]. The total absorbed radiative heat flux by *j*th layer in the PV cell emitted by the emitter, layer *s*, can be calculated as [81,86]:

$$Q_{sj} = \int_0^{\infty} \hbar\omega\{\psi(\omega, T_s, \mu_s) - \psi(\omega, T_j, \mu_j)\}\phi_{sj}(\omega)d\omega \tag{2.8}$$

And the rate of photogeneration in the j^{th} layer in the PV cell can be defined as [81]:

$$G_j = \sum_{l=0}^{m} \int_{\omega_g}^{\infty} \{\psi(\omega, T_l, \mu_l) - \psi(\omega, T_j, \mu_j)\}\phi_{lj}(\omega)d\omega \tag{2.9}$$

Where ω_g refers to the angular frequency of the band gap.

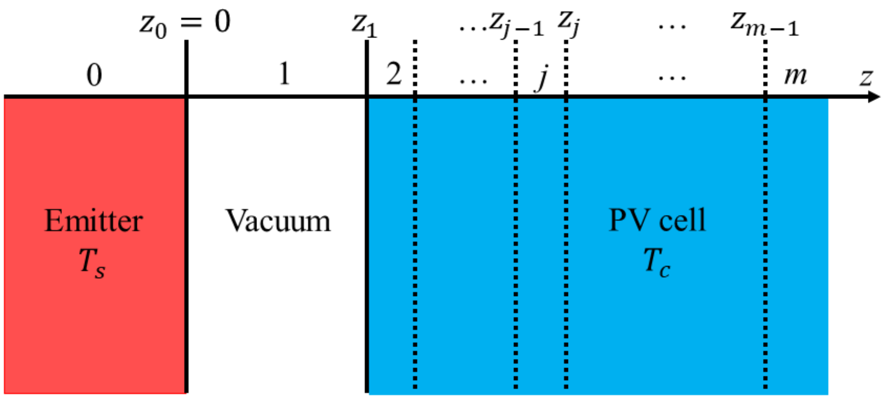

Fig. 2.4 The schematic of the layered TPV device. The TPV device is divided into m layers. Layer (0) is the emitting layer, layer (1) the vacuum gap layer and layers (2-m) form the PV cell. The emitting layer has a temperature of T_S and the PV cell has temperature of T_C.

2.1.4. Detailed Balance Model Used for Near-Field TPV Analysis

The detailed balance model comes from the Shockley-Queisser limit simulation [87]. This model has been frequently employed to determine the maximum efficiency of the photovoltaic cells. Following the pioneering work of Chen et al. [88], who were the first to employ the detailed balance analysis to a NF-TPV device by considering the non-radiative recombination rate, numerous research teams have utilized this model [49,89-91]. One significant feature of the detailed balance model lies in its ability to capture photon emission through radiative recombination using the Bose–Einstein distribution adjusted by the chemical potential μ [92]. In the detailed balance model is assumed that the quasi-Fermi levels are evenly distributed across the

PV cell as qV (i.e., $\mu = qV$). Another assumption in the detailed balance model is that any radiation absorbed by the cell with an energy level higher than the bandgap energy, creates EHPs that have contribution to the photocurrent (i.e., internal quantum efficiency is 100% for radiation with energies higher than the band gap energy). The equations utilized within this subsection are primarily generated from Refs. [81,89].

The equation to calculate current in the detailed balance model can be written as follows:

$$J(V) = q\{G_a - G_e(V) - R(V)\} \tag{2.10}$$

Where the rate of photogeneration per unit of area $G_a$can be defined as:

$$G_a = \sum_{j=2}^{m} \int_{\omega_g}^{\infty} \psi(\omega, T_s, 0)\phi_{sj}(\omega)\, d\omega \tag{2.11}$$

And the rate of radiative recombination rate per unit of area accompanied by the chemical potential $G_e(V)$ is as below:

$$G_e(V) = \sum_{j=2}^{m} \int_{\omega_g}^{\infty} \psi(\omega, T_c, \mu)\phi_{js}(\omega)\, d\omega \tag{2.12}$$

The non-radiative recombination rate $R(V)$ consists of three different terms: Auger, SRH bulk and surface recombination (i.e., $R(V) = R_{\text{Auger}} + R_{\text{SRH}} + R_{\text{surf}}$). The equations to find R_{Auger}, R_{SRH} and R_{surf} are explained in section 2.1.2 and its subsections. Each research study has uniquely determined $R(V)$ based on the specific non-radiative recombination rate types taken into account. In Ref. [91-92] only Auger and SRH non-radiative recombination are considered as they are dominant for the low band-gap material used in the PV cell. While, in Ref. [93] SRH non-radiative recombination is also neglected as it highly depends on the quality of the crystal and with employing high quality materials SRH recombination can be eliminated.

CHAPTER 3

ANALYZING EFFECT OF PRESENCE OF AIRGAP AND METAL COVER LAYER ON THE PERFORMANCE OF THE TPV DEVICE AND OPTIMIZING NOVEL TPV CONFIGURATIONS WITH HIGH POWER OUTPUT AND EFFICIENCY VALUES.

3.1. Different Methods to Enhance The Efficiency and Power Of TPV

As it was mentioned in section 2.1.1, η_c is an important metric to measure the TPV cell's performance. To obtain high values of η_c it is necessary to control the thermal emission reaching to the PV cell. As photon absorption with energy levels lower than the band gap of the cell does not contribute to photogeneration, improving the above band gap emission while suppressing the emission with energy levels below the band gap, results in η_c as well as P_e enhancements. An option to do this involves employing optical nanostructures at the scale of wavelengths into the thermal emitter. This effectively boosts the emissivity (or absorptivity) at specific resonant wavelengths [94-98]. An alternative method is utilizing reflectors and high-pass filters around the emitter to recycle low-energy photons effectively [99-102]. Placing a reflector as the last layer of the PV cell redirects the photons with energy levels lower than the band gap energy that does not have a contribution to photogeneration toward the emitter. Also, it increases the probability of the absorption of the functional photons with enough energy by the cell, that have not been absorbed by the cell through their first passage. Consequently, the back side reflector recycles both below and above band gap photons which has been illustrated experimentally in Refs [72,101]. Back side reflectors enhance the absorption and minimize radiation leakage by their reflection and making it possible to utilize very thin cells without having considerable reduction in P_e. Reduction in cell thickness can result in lower rate of non-radiative losses, explained in section 2.1.2, as Auger and SRH recombination are dependent to the thickness of the cell. The back reflector can either be in direct contact with the PV cell or remain separate from it (i.e., non-contact back reflector). It has been shown in far-field configuration [72] and in near-field configuration [103-104] that introducing an airgap between the back reflector and PV cell (i.e., using non-contact back reflectors) can make greater enhancement in the η_c and P_e than in contact back reflectors. This enhancement is due to the reduction of photon absorption by the back reflectors. In Ref. [103], the whole TPV structure is placed between two non-contact reflectors (i.e., putting a reflector backside the emitter and one backside the PV cell). They found that by utilizing a reflector backside the emitter, the lost emission from the emitter toward the surroundings can be considerably reduced. In Refs [105-106], it is shown that introducing a metal or intermetallic compound (i.e., a chemical compound containing metal) can result in increasing the photon absorption in the PV cell. In Ref. [107], a thin layer of $TiSi_2$ is placed on the PV cell, which leads to optical coupling between $TiSi_2$ and the emitter layer (ITO), as their resonance frequency overlaps. This coupling effect introduces new high energy plasmon modes near the PV cell and increases its photon absorption. The reason for choosing $TiSi_2$ instead of pure metals is that the metal's resonance frequency is much higher than that of ITO, and this causes weak optical coupling. In Ref. [49], the PV cell is covered by a very thin layer of Pt, which causes the absorption by the InAs cell to increase due to the generation of thermally excited plasmon resonances in the metal layer. They utilized a thin metal layer to decrease its reflection effect and increase the probability that the photons reach the PV layer. Their result showed that introducing a thin Pt layer on the PV cell results in threefold amplification in the power output of the system, from 11 to 31 W/cm^2.

So, placing an airgap between the back side reflector and the PV cell can enhance the η_c. On the other hand, introducing a metal or intermetallic compound on the surface of the PV cell can boost the radiation absorption by the PV cell and consequently increase the P_e. In the subsequent sections both options that improve the performance of the TPV device, are investigated thoroughly for a thin-film TPV device working on moderate temperature.

3.2. Analyzing Effect of Airgap and Thin Metal Cover on The Performance of TPV Devices

3.2.1. Effect of Airgap Between The Back Reflector and PV Cell on The Performance of The TPV Device

To examine the effect of the airgap between back reflector and the PV cell on the overall performance of the TPV cell, two structures are considered: one with airgap and the other with in-contact back reflector. The under-study structures are shown in Fig. 3.1. In both configurations ITO is used as the emitting layer due to its extensive accessibility and remarkable thermal endurance, withstanding temperatures as high as 1400 °C [108]. Additional reason is that the plasma frequency and damping rate of ITO can be adjusted by regulating the oxygen quantity during the deposition process [109]. This provides an opportunity to fine-tune the TPV system's performance and enhance its efficiency. The dielectric function of ITO is modeled by Drude model

$\varepsilon(\omega) = \varepsilon_\infty(1 - {\omega_p}^2/(\omega^2 + i\omega\Gamma))$, where $\varepsilon_\infty = 4$, $\omega_p = 0.4 - 0.9$ eV, and $\Gamma = 0.1 - 0.15$ eV [107]. In this section $\omega_p = 0.5$ eV, and $\Gamma = 0.1$ eV are used for the ITO layer. The resonance frequency can be calculated as $\omega_{\text{res}} \approx \omega_p\sqrt{\varepsilon_\infty/(\varepsilon_\infty + 1)}$. These selected properties are chosen to have a resonance frequency, 0.44 eV, slightly higher than the band gap of the PV cell, 0.354 eV. The mechanical support for thin-film ITO is considered to be Tungsten due to its high temperature stability. On the other side, a low band gap material, InAs, is utilized as PV cell's material which is frequently employed in TPV systems. The dielectric functions of InAs and tungsten are found from Ref. [110]. The back-side reflector is considered to be gold which has been considered as infinitely thick layer like the tungsten layer in the calculations. A Drude model is used to describe the dielectric function of gold, $\varepsilon(\omega) = 1 - {\omega_p}^2/(\omega^2 + i\omega\Gamma)$, where $\omega_p = 9.0241$ and $\Gamma = 0.0267$. The emitting layers, tungsten, and ITO are considered to have a uniform temperature of T_H and all the layers have temperature of T_c.

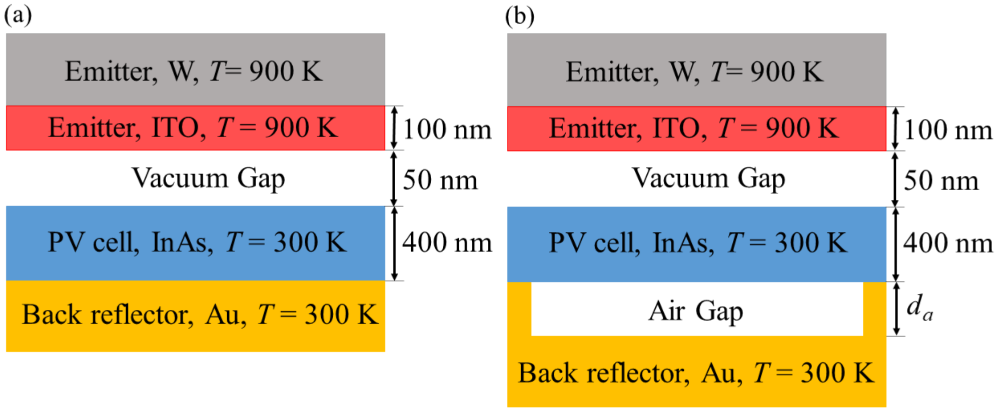

Fig. 3.1 (a) The TPV device with in-contact back reflector. (b) The TPV device with non-contact back reflector and an airgap between the back reflector and the PV cell with thickness of d_a.

3.2.1.1 Analyzing Model Explanation

Detailed balance model explained in section 2.1.4 is applied to analyze the TPV system. Eq. 2.1 is used to find the generated current in the external circuit. In Eq. 2.1 the term $R(V)$ can include 3 different terms, R_{Auger}, R_{SRH} and R_{surf}. However, the dominant nonradiative recombination terms in materials with low band gaps, like InAs, involve Auger and SRH recombination [93]. SRH recombination can be eliminated by enhancing the material's overall quality, Because of its reliance on crystal quality. Consequently, by utilizing a high-quality material, Auger recombination becomes the dominant part of the non-radiative recombination which can be found using Eq. 2.1, where n and p are, respectively, electron and hole concentrations which are voltage dependent. n and p can be calculated as [111]:

$$n = N_c \exp\left(\frac{E_{F,n} - E_c}{KT_c}\right) \tag{3.1}$$

$$p = N_v \exp\left(\frac{E_v - E_{F,P}}{KT_c}\right) \tag{3.2}$$

Where, $E_{F,n/P}$ refer to electrons and holes quasi-Fermi levels. In the detailed balance model, they are considered to be constant throughout the PV cell. Considering the applied voltage V, $V = E_{F,n} - E_{F,P}$. $E_{F,n}$ can be calculated with charge neutrality condition throughout the PV cell. $E_{c,v}$ stands for, respectively, conduction- and valence-band edges. $E_{F,n}$ and $E_{F,P}$ can be determined using equation below:

$$E_{F,n} = \frac{KT}{2}(-\ln N_c + \ln N_v - \ln N_A + \ln N_D) + \frac{1}{2}(E_c + E_v + V) \tag{3.3}$$

$$E_{F,P} = E_{F,n} - V \tag{3.4}$$

Where, $N_{c,v}$ are effective density states in conduction- and valence-band, respectively, and $N_{A,D}$ are density of acceptor and donor charge carries. The details of how to derive Eq. 3.3 is explained in Appendix A. In the current study Auger and SRH recombination are considered. All the needed information of InAs to calculate Auger and SRH recombination rates including $E_{c,v}$, $N_{c,v}$ and $N_{A,D}$ are listed in Table. 3.1 [49].

Table 3.1 Different parameters needed to calculate non-radiative recombination rates.

Coefficient	**Value**	**Coefficient**	**Value**
N_c [cm^{-3}]	8.7×10^{16}	E_c [eV]	0.354
N_v [cm^{-3}]	6.6×10^{18}	E_v [eV]	0
N_D [cm^{-3}]	2×10^{16}	n_i [cm^{-3}]	6.06×10^{14}
τ [ns]	100	$C_e = C_h$ [cm^{6}s^{-1}]	2.26×10^{-27}

3.2.1.2. Airgap Analysis Results and Discussions

In TPV devices it is necessary to minimize the radiation absorption by other layers than the PV cell layer. As only the radiation with energy levels higher than the bandgap of the cell absorbed by the PV cell contribute to the photocurrent generation. Defining an airgap between the back reflector and the PV cell can enhance the reflection of the unabsorbed radiation toward the emitter. In Fig 3.2 it is shown that with increasing the thickness of the airgap, the in-band (q_u) and out-of-band (q_l) radiation absorption by the metal reflector is decreased. It is due to the fact that the propagating waves are reflected back toward the emitter at the interface of the PV cell and airgap via total internal reflection. However, when the back reflector is in contact with the PV cell, the reflection is not perfect and some of the waves transmit from the PV cell to the back reflector and then become absorbed by the back reflector. It needs to be considered that to prevent the photon tunneling between the back reflector and the PV cell, the airgap thickness should be larger than the characteristic wavelength. Reduction in the radiation absorption by the metal back reflector results in a considerable boost in the conversion efficiency of the TPV device.

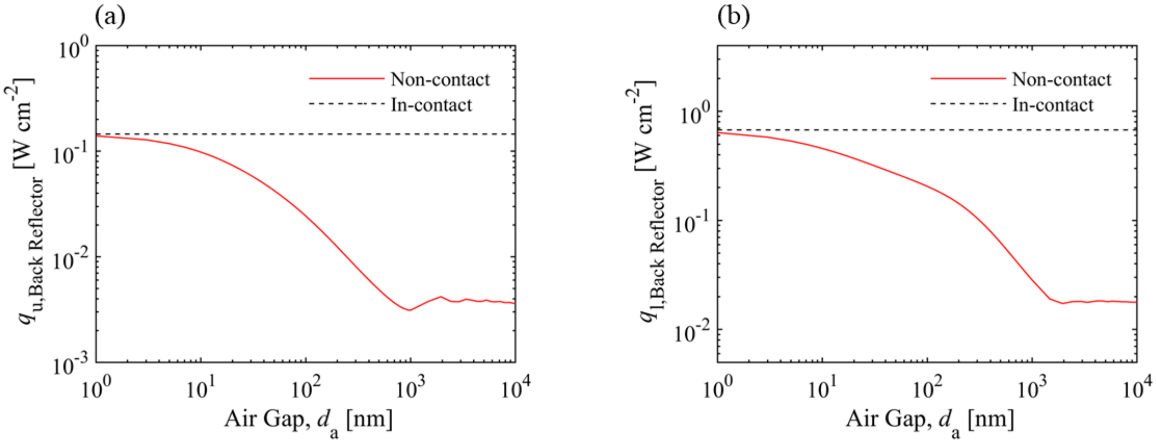

Fig. 3.2 (a) The in-band radiation absorption by the non-contact back reflector for different airgap sizes. The black sashed line shows the in-band radiation absorption by the in-contact back reflector. (b) The out-of-band radiation absorption by the non-contact back reflector for different airgap sizes. The black sashed line shows the out-of-band radiation absorption by the in-contact back reflector.

The effect of the airgap thickness on the radiation absorption by the PV cell layer is presented in Fig. 3.3. It can be seen that both in-band and out-of-band radiation absorption by the PV cell reduce by increasing the thickness of the airgap. Reduction in out-of-band radiation absorption by the PV cell leads to higher conversion efficiencies. However, the reduction in out-of-band absorption causes the power output to become smaller compared to in-contact back reflector configurations. The reason of higher absorption by the PV cell when it is in contact with the back reflector is that the in-contact back reflector causes the electric field (***E***) in the PV cell to grow. Metals can support surface plasmon resonances, which are collective oscillations of free electrons. These resonances can lead to enhancement in the local electromagnetic field near the metal surface. When the metal is in contact with the PV cell, plasmonic effects can lead to increased **E**-field and as a result absorption in the PV cell material. This higher absorption by the PV cell with in-contact back reflector results in higher power densities in the TPV cell, however, it is accompanied by higher radiation absorption by the metal reflector and as a result lower conversion efficiency.

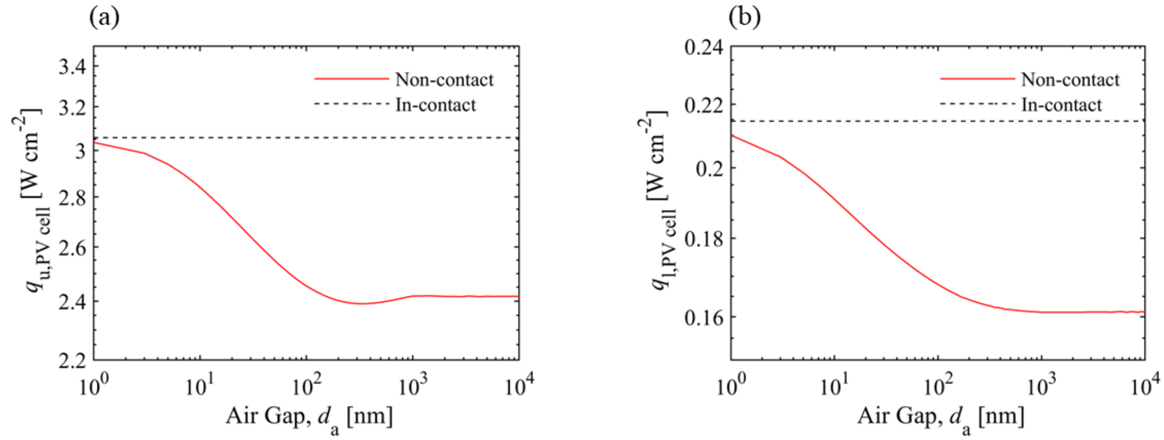

Fig. 3.3 (a) The in-band radiation absorption by the PV cell layer for different airgap sizes when the back reflector is non-contact. The black sashed line shows the in-band radiation absorption by the PV cell layer when the back reflector is in-contact. (b) The out-of-band radiation absorption by the PV cell layer for different airgap sizes when the back reflector is non-contact. The black sashed line shows the out-of-band radiation absorption by the PV cell layer when the back reflector is in-contact.

The variation of power output and the conversion efficiency of the TPV cell with respect to the airgap thickness is shown in Fig 3.4. With increasing the airgap thickness the radiation absorption by the metal back reflector decreases which causes the efficiency to increase. The efficiency of the configuration with 1000 nm airgap is about 4 percent (absolute value) higher than the case with in-contact back reflector. However, its power output decreases from 1.01 to 0.72 Wcm^{-2}. So, it is important to consider a trade-off between efficiency and power output to choose the airgap thickness as it does not have the same effect on both of them.

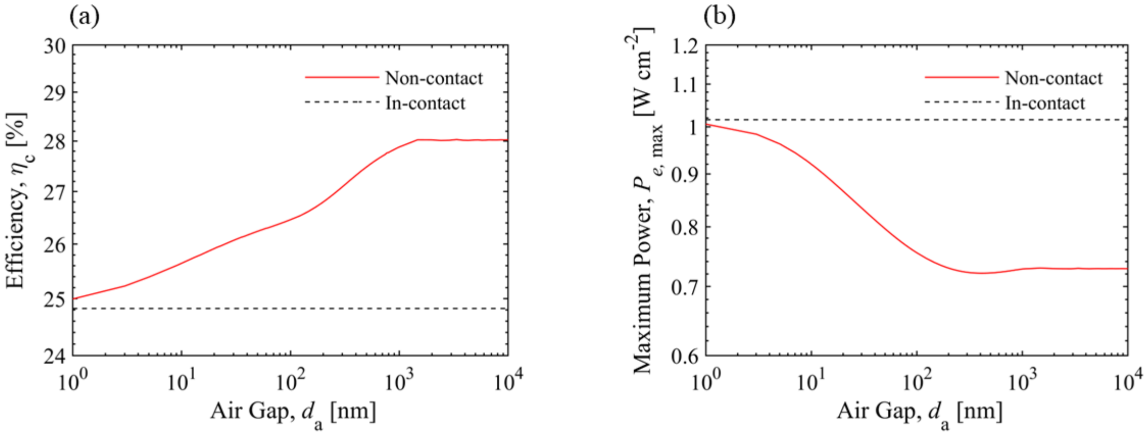

Fig. 3.4 (a) The efficiency of the TPV device for different airgap sizes when the back reflector is non-contact. The black sashed line shows the efficiency of the TPV device when the back reflector is in-contact. (b) The power output of the TPV device for different airgap sizes when the back reflector is non-contact. The black sashed line shows the power output of the TPV device when the back reflector is in-contact.

3.2.2. Effect of The Metal Cover on The Performance of The TPV Device

To investigate the effect of the metal cover on the overall performance of the TPV cell two structures shown in Fig 3.5 are considered. Configuration shown in Fig. 3.5(a) is the same as the structure shown in Fig 3.1(a). One cover metal layer, Cu, is added on top of the PV cell with thickness of t_m. Thicknesses and properties of all other layers are the same as what explained in section 3.2.1 and its subsections. A Drude model is used to describe the dielectric function of Coper, $\varepsilon(\omega) = 1 - {\omega_p}^2/(\omega^2 + i\omega\Gamma)$, where $\omega_p = 7.3917$ and $\Gamma = 0.00908$ [112]. Like what explained in section 3.2.1.1 detailed balance model is used to model the TPV system.

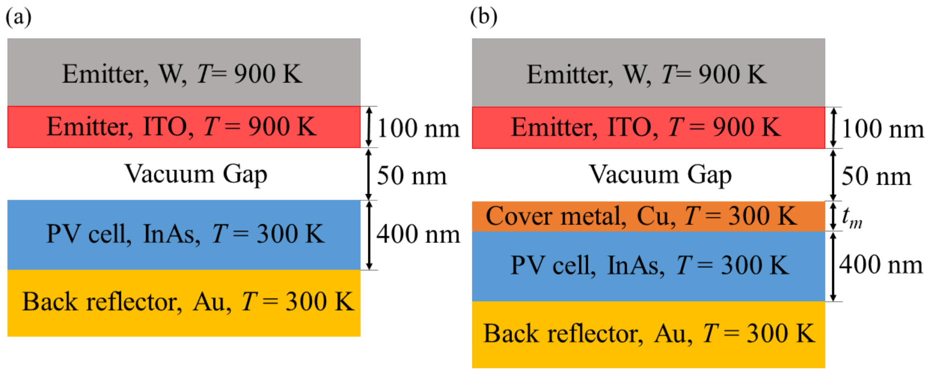

Fig. 3.5 (a) The schematic of the TPV device with an in-contact back reflector. (b) The schematic of the TPV device with an in-contact back reflector and a thin metal cover layer with thickness of t_m on top of the PV cell layer.

3.2.2.1. Metal Cover Analysis Results and Discussions

The radiation absorption by the PV cell can go up by increasing $|\boldsymbol{E}|^2$, where $\boldsymbol{E}$ is the electric field in the PV cell. So, one way to increase the power density of the TPV cell is to increase the electric field in the PV cell layer. The SPPs along the interface of the emitting layer, ITO, and the vacuum layer are evanescence due to their substantial parallel wavevectors. Consequently, the mode profile diminishes exponentially as one moves away from the emitter surface. As the PV cell is located at a distance from the surface of the ITO layer, the radiation absorption within the cell is just influenced by the evanescent tail of the electric field associated with the SPP which is shown in Fig 3.6(a). To maximize the benefits of the intense electric field created by surface resonances, it is necessary to have these resonances as close as possible to the PV cell layer which can be done by introducing a thin metal layer on top of the PV cell layer. Two structures are considered to investigate the effect of thin metal cover layer on the radiation absorption of the PV cell, which are shown in In Fig 3.6(a) and (b). Transmission function (ξ) from the emitting layer to the absorbing layer which determines the amount of absorbed radiation, explained how to obtain in Appendix B, is plotted as a function of k_ρ and ω for three cases: PV cell layer in in structure a (Fig 3.6(c)), PV cell layer including the cover metal layer in structure b (Fig 3.6(d)) and PV cell layer without cover metal layer in structure b (Fig 3.6(e)). The extra branch appeared in Fig 3.6(d) at low frequencies compared to two other cases is related to the metal cover layer. Thermal excitation of SPPs can occur at the interfaces of metal cover layer and vacuum and metal cover layer and PV cell layer, just like the SPPs observed at the vacuum and emitting layer, ITO, interface. Comparing Fig 3.6(e) and 3.6(c) it is clear that presence of cover metal layer caused the transmission function from emitter to the PV cell layer to be increased at the vicinity of the band gap. This enhancement results in higher in-band absorption by the PV cell layer and as a result higher power output of the TPV cell.

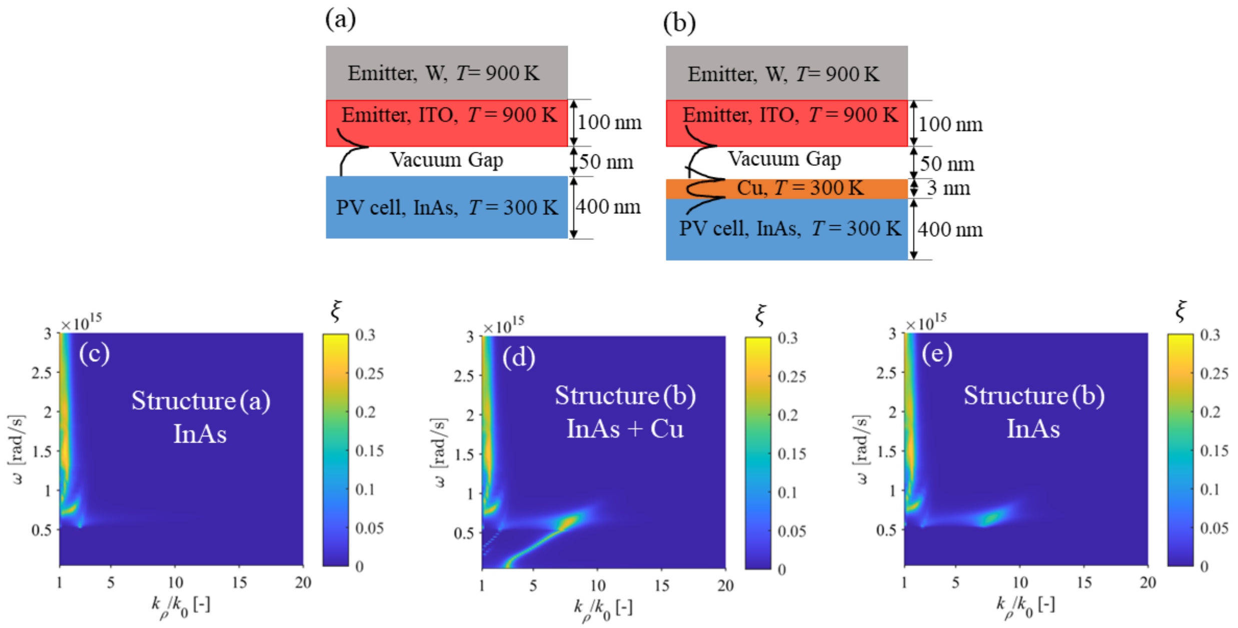

Fig. 3.6 Schematic of the TPV cell (a) with and (b) without thin Cu cover layer. (c,d,e) The transmission function values versus ω and k_ρ where k_ρ values are normalized by $k_0 = \omega/c_0$ where c_0 is the speed of the light in vacuum. The transmission coefficient of the PV cell shown in panel (a) is plotted in (c) and the transmission coefficient of the PV cell shown in panel (b) with and without the Cu cover layer are presented in (d) and (e), respectively.

In Fig. 3.7 the in-band and out-of-band radiation absorption by the PV cell is represented for different thicknesses of the metal cover. It can be seen that both in-band and out-of-band absorption decreases considerably for high metal cover thicknesses. It is due to the fact that the metals are highly reflective and at high thicknesses they reflect or absorb the radiations and prevent them from reaching and absorbed by the PV cell. However, at low thicknesses (<10 nm), the in-band absorption by the PV cell increases considerably which can result in a boost in the power density of TPV device. The absorbed in-band radiation by the PV cell for 2 nm metal cover reaches to 12.31 [Wcm^{-2}] compared to 3.06 [Wcm^{-2}] for a case without metal cover.

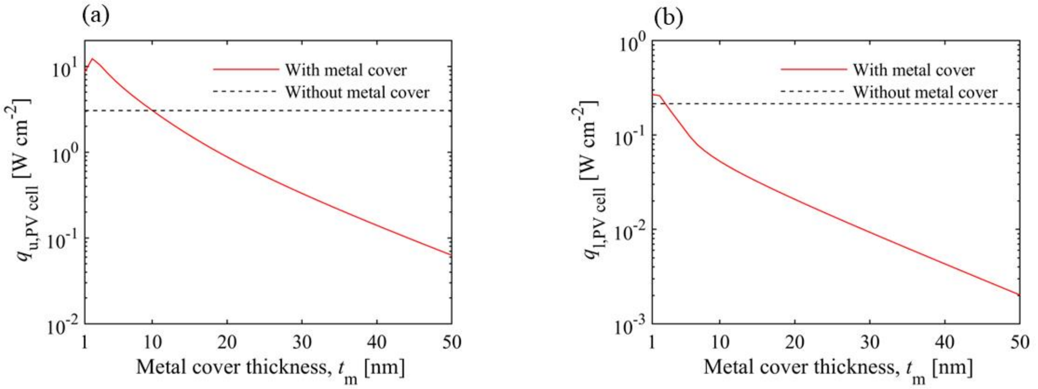

Fig. 3.7 (a) The in-band radiation absorption by the PV cell layer for different metal cover thicknesses. The black sashed line shows the in-band radiation absorption by the PV cell layer for a configuration without thin metal cover. (b) The out-of-band radiation absorption by the PV cell layer for different metal cover thicknesses. The black sashed line shows the out-of-band radiation absorption by the PV cell layer for a configuration without thin metal cover.

The configurations with metal cover, exhibit lower conversion efficiencies compared to the structures without metal cover as a considerable amount of radiations toward the PV cell are absorbed by the metal cover. In Fig 3.8(a) it is shown that by increasing the metal cover thickness the efficiency decreases considerably. On the other hand, as indicated in Fig 3.8(b) the power output of the TPV device can experience a boost by introducing a very thin metal cover (<10 nm) on top of the PV cell. By putting a thin Cu layer with a thickness of 2 nm on top of the PV cell, the power output of the TPV device goes up from 1.01 [Wcm^{-2}] to 4.84 [Wcm^{-2}], while the conversion efficiency decreases from 24.82% to 17.11%. Although, metal cover on top of the PV cell results in a reduction in the conversion efficiency, it is worthwhile due to the considerable enhancement it brings to power output. However, the thickness of the metal cover needs to be selected very carefully to achieve a reasonable tradeoff between efficiency and power output of the TPV system.

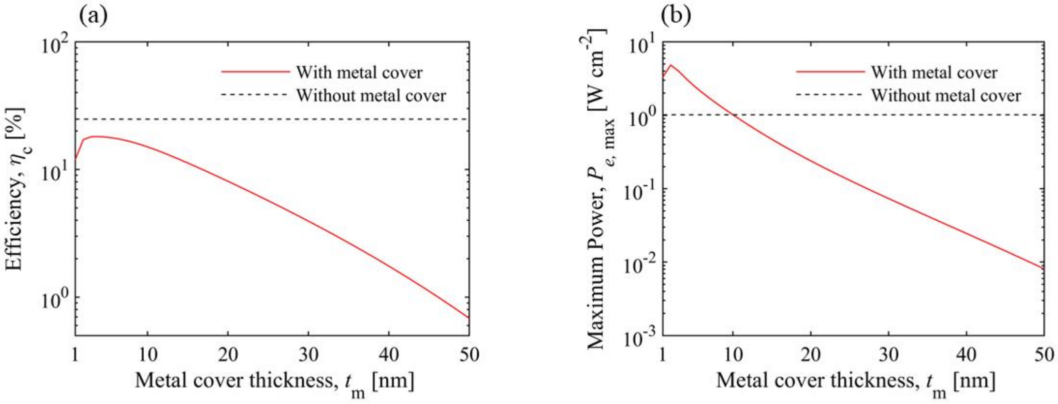

Fig. 3.8 (a) The efficiency of the TPV cell for different metal cover thicknesses. The black sashed line shows the efficiency for a configuration without thin metal cover. (b) The power output values for different metal cover thicknesses. The black sashed line shows the power output value for a configuration without thin metal cover.

3.3. TPV Configuration Optimization Using Genetic Algorithm

In the last section, two methods for enhancing the performance of TPV devices are discussed; First, maintaining an airgap between the back reflector metal and the PV cell to improve the reflection of the out-of-band radiations toward the emitter and decrease the radiation absorption by the back reflector which results in increasing the conversion efficiency considerably. Second, introducing a very thin metal layer on top of the PV cell to cause a boost in radiation absorption by the PV cell and consequently improving the power output of the TPV device remarkably. As a considerable amount of the coming radiation toward the PV cell is absorbed by the cover metal layer, the conversion efficiency of the TPV device decreases. So, this method can be utilized in waste heat recovery and for cases where the power density is much more important than the high conversion efficiency. The aim of this section is to optimize and design two TPV structures, one using the airgap method to gain high efficiencies and the other employing both methods to obtain high power outputs and meanwhile a reasonable value for efficiencies.

For the optimization purpose, genetic algorithms which is frequently utilized to find the global optimum [113]. The genetic algorithm is utilized by implementing concepts such as population size, elite selection, crossover, and mutation. The population size shows the quantity of individuals within each successive generation. The individuals within the present generation are referred to as parents, while those in the next generation are named as offspring or children. Each individual is composed of distinct variables like layer thickness and the material type used in the layers. Through the iterative process, the following generation's population is created by elite offspring, crossover-generated offspring, and mutation-induced offspring. Elite offspring are the best individuals of the present generation, that are used in the subsequent generation. Elite offspring is selected based on values calculated from the objective function employing an individual's variables. Crossover offspring are made from the combination of independent variables from a pair of parent individuals. Mutation offspring emerge from the random alteration of independent variables within a single parent. In the current study as it was mentioned earlier two objective functions are considered, η_c and P_e. The determined parameter values of genetic algorithms, explained above, are listed in Table. 3.2.

Table 3.2 The selected values for different parameters of the Genetic algorithm.

Population size	**Elite count**	**Crossover fraction**	**Maximum number of generations**
400	0.05* Population size = 20	0.8	100

There are two metrices that show how the Pareto frontier sets are distributed: Average pareto distance and average pareto spread. The first metric indicates how far are the pareto set points are located from each other and smaller values shows that the generated optimal points are close to each other. On the other hand, the second metric show how well the generated optimal points are distributed over the 2D space; Higher values are preferred as indicating that the optimal points are well-distributed. The optimization algorithm is designed to stop when the difference between both the values of Average pareto distance and average pareto spread of two consecutive iterations are less than 0.01.

3.3.1. TPV Structure Design Exhibiting High Conversion Efficiency

The under-study structure is shown in Fig. 3.9 which consists of 7 layers in total. Starting from the topmost layer, the substrate for the ITO emitting layer needs to endure high temperatures. Two materials W or Si which are highly stable at high temperatures are selected to be used in the substrate layer. ITO is selected to be utilized in the emitting layer and its reason is explained in detail in section 3.2.1. Regarding its thickness, in Ref [49] it was shown that the power output and efficiency can be increased by the thickness of the ITO layer and become insensitive to it when ITO-thickness > 30nm. So, as ITO is widely available and increasing its thickness does not affect the total cost of the TPV device considerably, 100 nm is chosen for its thickness. 100 nm is selected to make the fabrication process easier. The next layer is the vacuum gap size between the emitter and the PV cell layer and its thickness is considered to be 50 nm to make it practical. InAs is selected as the PV cell material and its thickness is considered to vary between 10 to 100 nm. The reason for choosing this range is that the dominant non-radiative recombination rates (Auger and SRH) are linearly connected to the PV cell thickness and consequently the thickness of the PV cell needs to be small to gain high efficiency values. Next layer is the air gap between the PV cell and the back reflector. Its thickness is considered to be from 10 to 5000 nm. The next layer is the back reflector, and it can be selected from 7 metals: Pt, Au, Ag, Al, Ti, Co and Cu. Its thickness can vary from 10 to 1000 nm. The parameters needed to calculate the dielectric function of the metals are listed in Table 3.4 which are found from Ref [112]. The last layer is the mechanical substrate for the metal back reflector and like the upper substrate it can be selected from 2 materials, W or Si. All the decision variables and their bounds are listed in Table 3.3.

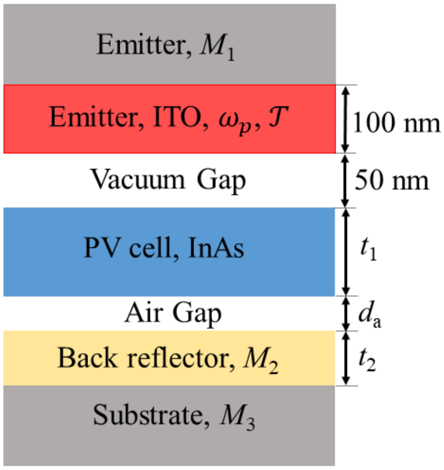

Fig. 3.9 The schematic of the TPV device equipped with an airgap layer between the back reflector and the PV cell layer. The configuration has 7 layers in total and 8 parameters that need to be optimized.

Table 3.3 The decision variables with their lower and upper bounds for TPV configuration equipped with an airgap between the back reflector and the PV cell layer.

Decision Variables	**Bounds**	**Intervals**	**Choices for materials**
M_1	[1 2]	1	W, Si
M_2	[1 7]	1	Pt, Au, Ag, Al, Ti, Co, Cu
M_3	[1 2]	1	W, Si
ω_p	[0.4 0.9] eV	0.01	-
$\mathcal{T}$	[0.1 0.15] eV	0.01	-
t_1	[10 100] nm	5	-
d_a	[10 5000] nm	10	-
t_2	[10 1000] nm	10	-

After the optimization is done, the algorithm provides a Pareto frontier which is shown in Fig 3.10. On the Pareto front, all points are optimum. Each point corresponds to a combination of the decision variables and objective function values. If the output power is the only deciding factor and the conversion efficiency is ignored, the optimal point become point B. Point A, alternatively, represents the system's best conversion efficiency regardless of output power. Two other points, the ideal point (IP) and the non-ideal point (NIP), are obtained when output power and conversion efficiency are both at their highest and lowest values, respectively. The best condition happens at point IP. So, it is necessary to find a condition that is closest to point IP. Technique for Order of Preference by Similarity to Ideal Solution (TOPSIS) method searches over the optimal points on the Pareto front and finds the point with the shortest geometric distance from IP and select it as the best optimum point which is point C in the Pareto frontier. The values for the decision variables as well as two objective functions for points A, B and C in the Pareto frontier are listed in Table 3.5. Point C which has been selected as the most optimum point on the Pareto frontier exhibits 34.52 % and 0.53 [Wcm^{-2}] as the efficiency and the power output, respectively. From Table 3.5 it can be seen that with increasing t_1, the thickness of the PV cell, the efficiency decreases while the power output goes up. As it was explained mentioned before, to have high efficiency and power output values, it is necessary to decrease the radiation absorption by all the layers in the TPV device other than the PV cell layer. The dielectric function of the metals is modeled using a Drude model, $\varepsilon(\omega) = 1 - {\omega_p}^2/(\omega^2 + i\omega\Gamma)$. The absorption in the Drude model is determined by the imaginary part of the dielectric function, which is the term $i\omega\Gamma$. Higher Γ results in larger imaginary part of the dielectric function and consequently greater absorption by the metal layer. As it is clear from Table 3.4, the smallest Γ value belongs to Cu. So, Cu has smaller absorption compared to other considered metals. This is the reason that Cu has been selected as the back reflector metal by the optimization algorithm. All the points in Table 3.5 have lower power output values compared to the TPV configuration with in-contact back reflector which exhibits 30% and 1.2 Wcm^{-2} for efficiency and power output, respectively. To gain high power output and efficiency simultaneously, it is needed to decrease the vacuum gap size. The TPV configuration with 10 nm vacuum gap size and equipped with non-contact back reflector can reach to 48% and 12.5 Wcm^{-2} compared to 40% and 10 Wcm^{-2} of the case with in-contact back reflector.

Table 3.4 Drude model parameters of the metals needed to calculate the dialectic function.

Material Name	**Au**	**Ag**	**Cu**	**Ti**	**Pt**	**Al**	**Co**
ω_p (eV)	9.0241	9.0109	7.3917	2.5144	5.145	14.757	3.969
Γ (eV)	0.0267	0.018	0.00908	0.0474	0.069	0.0818	0.0366

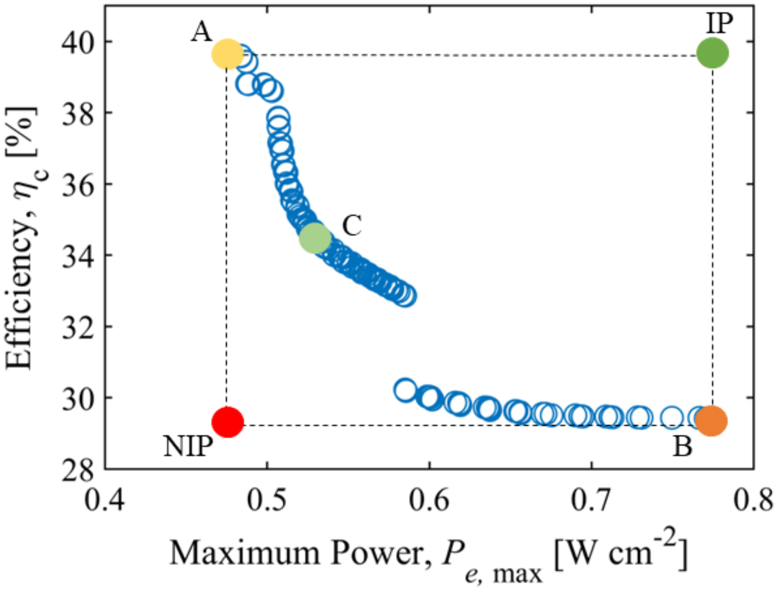

Fig. 3.10 The Pareto frontier that contains all the optimum points (Pareto set) for the TPV configuration equipped with air gap. If the output power is the only deciding factor and the conversion efficiency is ignored, the optimal point become point B. Point A, alternatively, represents the system's best conversion efficiency regardless of output power. Two other points, the ideal point (IP) and the non-ideal point (NIP), are obtained when output power and conversion efficiency are both at their highest and lowest values, respectively. Point C is the most optimum point found by TOPSIS method.

Table 3.5 The optimized values of the decision variables for points A, B and C on the Pareto frontier.

Point	M_1	M_2	M_3	ω_p **[eV]**	$\mathcal{T}$ **[ev]**	t_1 **[nm]**	d_a **[nm]**	t_2 **[nm]**	**Efficiency [%]**	**Power output [Wcm^{-2}]**
A	W	Cu	Si	0.47	0.1	10	1310	400	39.64	0.48
B	Si	Cu	W	0.51	0.1	100	620	640	29.35	0.77
C	W	Cu	W	0.49	0.1	55	1260	550	34.52	0.53

3.3.2. TPV Structure Design with High Power Output For Waste Heat Recovery Applications

The under-study structure is shown in Fig. 3.11 which has 8 layers in total. All the decision variables and their values are explained in the last section. The only difference between this structure and the structure presented in Fig. 3.9 is a thin metal layer on top of the PV cell layer. The metal cover can be selected from 7 metal choices like the back reflector. Regarding its thickness, it can vary from 3 to 10 nm. Although in section 3.2.2.1 the lower bound for the thickness of the cover metal is considered to be 1 nm and the highest power output is gained when metal cover has thickness of 2 nm (indicated in Fig 3.8(b)), the lower bound for the optimization process is selected to be 3 nm to make the fabrication process easier and make the TPV structure more practical. Very thin layer metal fabrication on different mechanical supports has been experimentally done already [114-115]. All the decision variables and their bounds are listed in table 3.6.

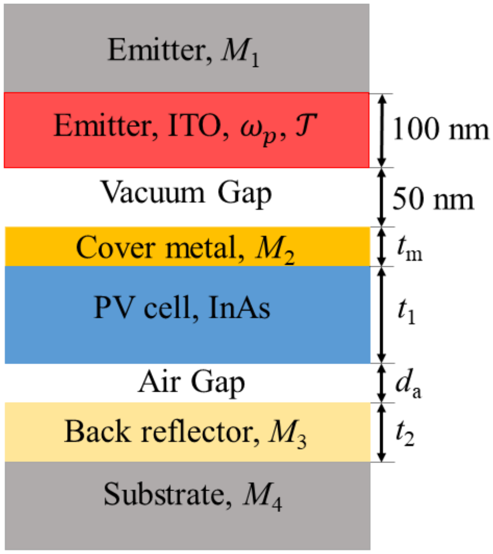

Fig. 3.11 The schematic of the TPV device equipped with an airgap layer between the back reflector and the PV cell layer and a thin metal layer on top of the PV cell layer. The configuration has 8 layers in total and 10 parameters that need to be optimized.

Table 3.6 The decision variables with their lower and upper bounds for TPV configuration equipped with an airgap between the back reflector and the PV cell layer and a thin metal cover layer on top of the PV cell layer.

Decision Variables	**Bounds**	**Intervals**	**Choices for materials**
M_1	[1 2]	1	W, Si
M_2	[1 7]	1	Pt, Au, Ag, Al, Ti, Co, Cu
M_3	[1 7]	1	Pt, Au, Ag, Al, Ti, Co, Cu
M_4	[1 2]	1	W, Si
ω_p	[0.4 0.9] eV	0.01	-
$\mathcal{T}$	[0.1 0.15] eV	0.01	-
t_{m}	[3 10] nm	1	-
t_1	[10 100] nm	5	-
d_{a}	[10 5000] nm	10	-
t_2	[10 1000] nm	10	-

The Pareto frontier is presented in Fig 3.12. There are 5 points, IP, NIP, A, B and C highlighted on the Pareto frontier. The decision variables in addition to the objective function values for points A, B and C are listed in Table 3.7. As it was explained in the last section, Cu has the smallest Γ and radiation absorption between all the considered metals which has been selected to be used in the back reflector layer. Regarding the thin metal cover, it can be seen that Cu with thickness of 3 nm results in the highest efficiency value, point A on the Pareto frontier. Regarding its thickness, as it has been shown in Fig 3.8 the power output and efficiency values decreases dramatically at higher metal cover thicknesses. It is due to the fact that higher thicknesses of the metal covers are accompanied by higher absorption and reflection of them and less radiation reaching the PV cell layer. Therefore, the low bound value for t_1, 3nm, is considered as the thickness of the metal cover layer. Points B and C on the Pareto frontier, have Co with thickness of 3 nm as the thin metal cover layer which results in higher power output values compared to point A. The reason of higher power output values with using Co rather than Cu is that the resonance frequency of Co is lower and closer to the resonance frequency of ITO which causes stronger optical coupling and consequently higher radiation absorption by the PV cell. On the other hand, Co has higher Γ and as a result higher radiation absorption which leads to decreasing the efficiency. As it can be seen from Table 3.4 the resonance frequency of Ti is the lowest between all considered metals. However, its higher Γ value compared to Co caused the efficiency to go down and Ti not be chosen as the best choice for the metal cover layer. Although the goal of this section has been to design a TPV structure with high power output value, the structure A might be preferable to the other two configurations. As it has high efficiency while exhibiting a high power output value.

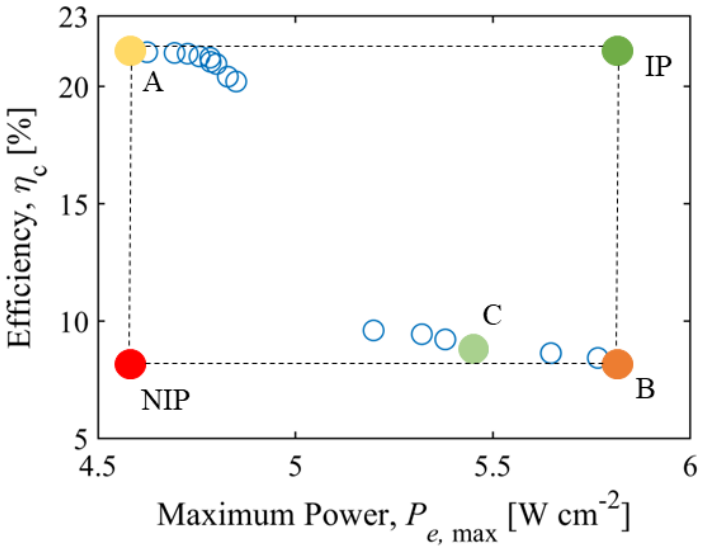

Fig. 3.12 The Pareto frontier that contains all the optimum points (Pareto set) for the TPV configuration equipped with air gap and metal cover simultaneously.

Table 3.7 The optimized values of the decision variables for points A, B and C on the Pareto frontier.

Point	M_1	M_2	M_3	M_4	ω_p **[eV]**	$\mathcal{T}$ **[ev]**	t_m **[nm]**	t_1 **[nm]**	d_a **[nm]**	t_2 **[nm]**	**Efficiency [%]**	**Power output [Wcm^{-2}]**
A	W	Cu	Cu	Si	0.58	0.1	3	60	2860	310	21.47	4.59
B	W	Co	Cu	W	0.5	0.1	3	15	1310	800	8.16	5.81
C	W	Co	Cu	Si	0.53	0.1	3	15	1200	790	8.78	5.46

CONCLUSION

In this study different methods for enhancing the performance, efficiency and power output, of the NF-TPV devices were thoroughly investigated and different NF-TPV configurations were designed. The main outcomes of the study are as follows:

- Placing an airgap between the PV cell and the back metal reflector causes the efficiency to go up considerably but results in lower power output values. To maintain high power output and efficiency values simultaneously, it is necessary to have small vacuum gap sizes, ≈ 10 nm. A NF-TPV configuration with 10 nm vacuum gap size and 900 K emitter equipped with non-contact back reflector can reach power output and efficiency of 12.5 Wcm^{-2} and 48% compared to 10 Wcm^{-2} and 40% for in-contact back reflector, respectively.
- Introducing a very thin metal layer on top of the PV cell layer increases the power output of the NF-TPV devices tremendously. The power output of a NF-TPV structure with 50 nm vacuum gap size and 900 K emitter equipped with a 3 nm Cu metal cover can increase nearly by a factor of 4, from 1.2 Wcm^{-2} to 4.59 Wcm^{-2}. On the other hand, the efficiency decreases with introducing a thin metal cover. So, this method is appropriate for cases where power output is much more important than the efficiency.
- Closer plasma frequency (ω_p) of the thin metal cover results in stronger coupling effect between the emitter and the metal cover layer and consequently, greater enhancement in the in-band absorption by the PV cell. This results in higher power output values.
- Absorption of a metal layer is related to the imaginary part of the dielectric function. So, Smaller damping ratio Γ causes the imaginary part of the dielectric function to decrease and as a result absorption by the metal layer goes down. Reduction in absorption by the metal layer leads to increasing the efficiency of the TPV device.

FUTURE WORKS

- Placing a thin metal layer on top of the PV cell causes the power output of the TPV device to go up. However, the efficiency experiences a considerable reduction due to very high absorption by the metal cover layer. It would be good to find a replacement for the metal covers with low absorption. Finding a material that increases the in-band absorption of the PV cell, like what metal cover do, but with lower absorption compared to metals. As a result, TPV device can have high efficiency and power output simultaneously.
- It was shown that placing an air gap between the PV cell and the back reflector can enhance the efficiency and in some cases the power output. For modeling the air gap, a layer of vacuum is considered like what exist between the emitter and the PV cell. It would be more realistic to use the properties of the air in simulations of the air gap layer.
- The temperature of the PV cell needs to be kept at room temperature to minimize generating unwanted electric currents in the PV cell. One of the ways to remove heat from the PV cell is to place the heat sink in-contact with the back reflector of PV cell. It would be a good effort to study about an efficient way to remove heat from the PV cell when it has an air gap at the backside.

APPENDICES

APPENDIX A: ELECTRON AND HOLE QUASI-FERMI LEVELS DETERMINATION VIA CHARGE NEUTRALITY OVER THE PV CELL'S THICKNESS

n and p can be calculated using equations below[111]:

$$n = N_c \exp\left(\frac{E_{F,n} - E_c}{KT_c}\right) \tag{A(1)}$$

$$p = N_v \exp\left(\frac{E_v - E_{F,P}}{KT_c}\right) \tag{A(2)}$$

The charge neutrality over the PV cell's thickness says that:

$$n + N_A = p + N_D \tag{A(3)}$$

With plugging Eq. A(1-2) into Eq. A(3), replacing $E_{F,P}$ with $E_{F,n} - V$ we have:

$$N_c \exp\left(\frac{E_{F,n} - E_c}{KT_c}\right) - N_v \exp\left(\frac{E_v - E_{F,n} + V}{KT_c}\right) + N_A - N_D = 0 \tag{A(4)}$$

The objective is to find a voltage dependent equation for $E_{F,n}$. With using natural logarithm, Eq. A(4) can be simplified to:

$$\ln N_c + \frac{E_{F,n} - E_c}{KT_c} - (\ln N_v + \frac{E_v - E_{F,n} + V}{KT_c}) + \ln N_A - \ln N_D = 0 \tag{A(5)}$$

Finally $E_{F,n}$ and $E_{F,P}$ can be defined as:

$$E_{F,n} = \frac{KT}{2}(-\ln N_c + \ln N_v - \ln N_A + \ln N_D) + \frac{1}{2}(E_c + E_v + V) \tag{A(6)}$$

$$E_{F,P} = E_{F,n} - V \tag{A(7)}$$

APPENDIX B: TRANSMISSION COEFFICIENT FROM EMITTING LAYER TOWARDS THE ABSORBING LAYER

Fig. B1 two substrates that are separated vacuum layer with thickness of *D*. The thickness and corresponding dielectric function of the layers are indicated with t_1 and t_3 and $\varepsilon_{r,1}$ and $\varepsilon_{r,3}$, respectively. The temperatures of the substrates are T_1 and T_3, respectively, where $T_1 \neq T_3$. The wanted value is $q_{\text{tot},13}$, the overall near-field radiative heat flux transferring from medium 1 to 3. With Integrating the spectral (i.e., frequency dependent) heat flux, $q_{\omega,13}$, for all frequencies the overall heat flux can be calculated as:

$$q_{\text{tot},13} = \int_0^\infty q_{\omega,13} d\omega \qquad \text{B(1)}$$

where the spectral heat flux can be found using the framework of fluctuational electrodynamics as [116]:

$$q_{\omega,13} = \frac{\Theta(\omega, T_1) - \Theta(\omega, T_3)}{4\pi^2} \sum_{\alpha=\text{TE, TM}} \left(\int_0^{k_0} \zeta_{\text{prop}}^{\alpha} k_\rho dk_\rho + \int_{k_0}^{\infty} \zeta_{\text{evan}}^{\alpha} k_\rho dk_\rho \right) \qquad \text{B(2)}$$

In Eq. 2, k_0 is the magnitude of the wavevector in the free space, k_ρ is the wavevector component that is oriented along the interface between the free space substrate, the superscript α refers to the transverse electric (TE) and the transverse magnetic (TM) polarization states, and $\zeta_{\text{prop}}^{\alpha}$ ($\zeta_{\text{evan}}^{\alpha}$) is the energy transmission function for propagating (evanescent) waves for α polarization. The quantity Θ in Eq. B(2) is the average energy of an electromagnetic state that corresponds to the frequency ω and temperature *T* and is calculated as:

$$\Theta(\omega, T) = \frac{\hbar\omega}{e^{\hbar\omega/k_B T} - 1} \qquad \text{B(3)}$$

where $\hbar$ and k_B are the reduced Planck's and Boltzmann constants, respectively. The transmission functions $\zeta_{\text{prop}}^{\alpha}$ and $\zeta_{\text{evan}}^{\alpha}$ are obtained as [116]:

$$\zeta_{\text{prop}}^{\alpha} = \frac{(1 - |R_{01}^{\alpha}|^2 - |T_{01}^{\alpha}|^2)(1 - |R_{03}^{\alpha}|^2 - |T_{03}^{\alpha}|^2)}{|1 - R_{01}^{\alpha} R_{03}^{\alpha} e^{i2k_{0z}D}|^2} \tag{B(3)}$$

$$\zeta_{\text{evan}}^{\alpha} = \frac{4\text{Im}(R_{01}^{\alpha})\text{Im}(R_{03}^{\alpha}) e^{-2\text{Im}(k_{0z}D)}}{|1 - R_{01}^{\alpha} R_{03}^{\alpha} e^{i2k_{0z}D}|^2} \tag{B(4)}$$

where k_{0z} is the z-component (as shown in Fig. B1, the z-axis is perpendicular to the interface of graphene and free space) of the wavevector in medium 0 (free space), and R_{0j}^{α} and T_{0j}^{α} are, respectively, the reflection and transmission coefficients of medium j when illuminated with an incident electromagnetic field from medium 0.

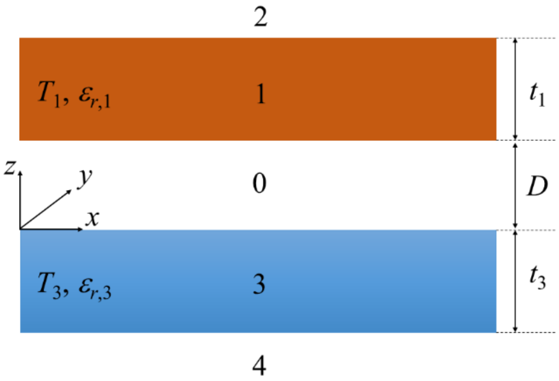

Fig. B.1 A schematic for the system under consideration. Two substrates (media 1 and 3) are separated by a layer of vacuum of thickness D. The substrates 1 and 3 have temperatures T_1 and T_3, thicknesses t_1 and t_3, and dielectric functions $\varepsilon_{r,1}$ and $\varepsilon_{r,3}$, respectively.

REFERENCES

[1] Modest, M. F. et al., (2003). Radiative heat transfer, 1, 1-29.

[2] Planck, M. (1914). Blakiston.

[3] Howell, J. R. et al., (2020). Thermal radiation heat transfer. CRC press.

[4] Zhang, Z. M. et al., (2007). Nano/microscale heat transfer (Vol. 410). New York: McGraw-Hill.

[5] Joulain, K. et al., (2005). Surface Science Reports, 57(3-4), 59-112.

[6] Rytov, S. M. et al., (1989). (Vol. 3, p. 115). Berlin: Springer.

[7] Francoeur, M. et al., (2009). Journal of Quantitative Spectroscopy and Radiative Transfer, 110(18), 2002-2018.

[8] Jackson, J. D. (1999). Classical electrodynamics john wiley & sons. Inc., New York, 13.

[9] DiMatteo, R. S. et al., (2001). Applied Physics Letters, 79(12), 1894-1896.

[10] Whale, M. D. et al., (2002). IEEE Transactions on Energy Conversion, 17(1), 130-142.

[11] Narayanaswamy, A. et al., (2003). Applied Physics Letters, 82(20), 3544-3546.

[12] Laroche, M. et al., (2006). Journal of applied physics, 100(6).

[13] Park, K. et al., (2007). In RADIATIVE TRANSFER-V. Proceedings of the Fifth International Symposium on Radiative Transfer. Begel House Inc.

[14] Francoeur, M. et al., (2011). IEEE Transactions on Energy Conversion, 26(2), 686-698.

[15] Ilic, O. et al., (2012). Optics express, 20(103), A366-A384.

[16] Bernardi, M. P. et al., (2015). Scientific reports, 5(1), 11626.

[17] Molesky, S. et al., (2015). Physical Review B, 91(20), 205435.

[18] Lau, J. Z. J. et al., (2016). Journal of Quantitative Spectroscopy and Radiative Transfer, 171, 39-49.

[19] St-Gelais, R. et al., (2017). ACS nano, 11(3), 3001-3009.

[20] Vongsoasup, N. et al., (2017). International Journal of Heat and Mass Transfer, 115, 326-332.

[21] Fiorino, A. et al., (2018). Nature nanotechnology, 13(9), 806-811.

[22] Lim, M. et al., (2018). Journal of Quantitative Spectroscopy and Radiative Transfer, 210, 35-43.

[23] Sabbaghi, P. et al., (2019). Journal of Quantitative Spectroscopy and Radiative Transfer, 234, 108-114.

[24] Bhatt, G. R. et al., (2020). Nature communications, 11(1), 2545.

[25] Milovich, D. et al., (2020). Journal of Photonics for Energy, 10(2), 025503-025503.

[26] Lucchesi, C. et al., (2021). Nano Letters, 21(11), 4524-4529.

[27] Guha, B. et al., (2012). Nano letters, 12(9), 4546-4550.

[28] Chen, K. et al., (2016). Physical Review Applied, 6(2), 024014.

[29] Zhu, L. et al., (2019). Nature, 566(7743), 239-244.

[30] Otey, C. R. et al., (2010). Physical review letters, 104(15), 154301.

[31] Basu, S. et al., (2011). Applied Physics Letters, 98(11).

[32] Iizuka, H. et al., (2012). Journal of Applied Physics, 112(2).

[33] Wang, L. P. et al., (2013). Nanoscale and microscale thermophysical engineering, 17(4), 337-348.

[34] Yang, Y. et al., (2013). Applied Physics Letters, 103(16).

[35] Joulain, K. et al., (2015). Optics express, 23(24), A1388-A1397.

[36] Ghanekar, A. et al., (2016). Applied Physics Letters, 109(12).

[37] Zheng, Z. et al., (2017). International Journal of Heat and Mass Transfer, 109, 63-72.

[38] Fiorino, A. et al., (2018). ACS nano, 12(6), 5774-5779.

[39] Ghanekar, A. et al., (2018). Optics express, 26(2), A209-A218.

[40] Wen, S. et al., (2019). Journal of Quantitative Spectroscopy and Radiative Transfer, 234, 1-9.

[41] Wen, S. et al., (2019). Journal of Quantitative Spectroscopy and Radiative Transfer, 234, 1-9.

[42] Xu, G. et al., (2020). International Journal of Thermal Sciences, 149, 106179.

[43] Mittapally, R. et al., (2021). Nature communications, 12(1), 4364.

[44] Landrieux, S. et al., (2022). Applied Physics Letters, 120(14).

[45] De Wilde, Y. et al., (2006). Nature, 444(7120), 740-743.

[46] Jones, A. C. et al., (2012). Nano letters, 12(3), 1475-1481.

[47] Recovery, W. H. (2008). US Department of Energy, Prepared by BCS, Incorporated.

[48] Mulet, J. P. et al., (2002). Microscale Thermophysical Engineering, 6(3), 209-222.

[49] Zhao, B. et al., (2017). Nano Energy, 41, 344-350.

[50] Liu, W. et al., (2015). Acta Materialia, 87, 357-376.

[51] Ovik, R. et al., (2016). Renewable and sustainable energy reviews, 64, 635-659.

[52] Wedlock, B. D. (1963). Proceedings of the IEEE, 51(5), 694-698.

[53] Becquerel, M. E. (1839). Comptes rendus hebdomadaires des séances de l'Académie des sciences, 9, 561-567.

[54] Licht, A. et al., (2019). MRS Advances, 4(41-42), 2271-2282.

[55] Fraas, L. M. et al., (2003). Semiconductor Science and Technology, 18(5), S247.

[56] Lenert, A. et al., (2014). Nature nanotechnology, 9(2), 126-130.

[57] Narayanaswamy, A. et al., (2003). Applied Physics Letters, 82(20), 3544-3546.

[58] Laroche, M. et al., (2006). Journal of applied physics, 100(6).

[59] Park, K. et al., (2007). Proceedings of the Fifth International Symposium on Radiative Transfer. Begel House Inc.

[60] Ilic, O. et al., (2012). Optics express, 20(103), A366-A384.

[61] St-Gelais, R. et al., (2017). ACS nano, 11(3), 3001-3009.

[62] Zhao, B. et al., (2018). Nano letters, 18(8), 5224-5230.

[63] Ben-Abdallah, P. et al., (2019). Zeitschrift für Naturforschung A, 74(8), 689-696.

[64] Fiorino, A. et al., (2018). Nature nanotechnology, 13(9), 806-811.

[65] DiMatteo, R. S. et al., (2001). Applied Physics Letters, 79(12), 1894-1896.

[66] Whale, M. D. et al., (2002). IEEE Transactions on Energy Conversion, 17(1), 130-142.

[67] Laroche, M. et al., (2006). Journal of applied physics, 100(6).

[68] Park, K. et al., (2007). Proceedings of the Fifth International Symposium on Radiative Transfer. Begel House Inc.

[69] Francoeur, M. et al., (2011). IEEE Transactions on Energy Conversion, 26(2), 686-698.

[70] Bernardi, M. P. et al., (2015). Scientific reports, 5(1), 11626.

[71] Omair, Z. et al., (2019). Proceedings of the National Academy of Sciences, 116(31), 15356-15361.

[72] Fan, D. et al., (2020). Nature, 586(7828), 237-241.

[73] Tong, J. K. et al., (2015). Scientific reports, 5(1), 10661.

[74] Bright, T. J. et al., (2014). Journal of Heat Transfer, 136(6), 062701.

[75] Zhao, B. et al., (2018). Nano letters, 18(8), 5224-5230.

[76] Datas, A. et al., (2021). In Ultra-high temperature thermal energy storage, transfer and conversion (pp. 285-308). Woodhead Publishing.

[77] Philipps, S. P. et al., (2018). In McEvoy's handbook of photovoltaics (pp. 439-472). Academic Press.

[78] Goetzberger, A. et al., (1998). Crystalline silicon solar cells (Vol. 1, pp. 114-118). Chichester: Wiley

[79] Green, M. A. (1982). Englewood Cliffs.

[80] Song, B. et al., (2015). Nature nanotechnology, 10(3), 253-258.

[81] Feng, D. et al., (2021). Journal of Applied Physics, 129(21).

[82] Nelson, J. A. (2003). World Scientific Publishing Company.

[83] Francoeur, M. et al., (2009). Journal of Quantitative Spectroscopy and Radiative Transfer, 110(18), 2002-2018.

[84] Callahan, W. A. et al., (2021). Physical Review Applied, 15(5), 054035.

[85] Joulain, K. et al., (2005). Surface Science Reports, 57(3-4), 59-112.

[86] Tervo, E. et al., (2018). Frontiers in Energy, 12, 5-21.

[87] Shockley, W. (1961). The Shockley-Queisser limit. J. Appl. Phys, 32(3), 510-519.

[88] Chen, K. et al., (2015). Applied Physics Letters, 107(9).

[89] DeSutter, J. et al., (2017). Physical Review Applied, 8(1), 014030.

[90] Feng, D. et al., (2020). Nanoscale and Microscale Thermophysical Engineering, 24(1), 1-19.

[91] Papadakis, G. T. et al., (2020). Nano Letters, 20(3), 1654-1661.

[92] Song, J. et al., (2022). Solar Energy Materials and Solar Cells, 238, 111556.

[92] Chen, K. et al., (2017). Journal of Applied Physics, 122(14).

[93] Papadakis, G. T. et al., (2021). Physical Review Applied, 16(6), 064063.

[94] Inoue, T. et al., (2015). Optica, 2(1), 27-35.

[95] De Zoysa, M. et al., (2012). Nature Photonics, 6(8), 535-539.

[96] Rinnerbauer, V. et al., (2013). Optics express, 21(9), 11482-11491.

[97] Dyachenko, P. N. et al., (2016). Nature communications, 7(1), 11809.

[98] Asano, T. et al., (2016). Science advances, 2(12), e1600499.

[99] Ilic, O. et al., (2016). Nature nanotechnology, 11(4), 320-324.

[100] Bierman, D. M. et al., (2016). Nature Energy, 1(6), 1-7.

[101] Omair, Z. et al., (2019). Proceedings of the National Academy of Sciences, 116(31), 15356-15361.

[102] Fan, D. et al., (2020). Nature, 586(7828), 237-241.

[103] Inoue, T. et al., (2021). Optics Express, 29(7), 11133-11143.

[104] Feng, D. et al., (2022). Solar Energy Materials and Solar Cells, 237, 111562.

[105] Gee, J. M. et al., (2002, May). In Conference Record of the Twenty-Ninth IEEE Photovoltaic Specialists Conference, 2002. (pp. 896-899). IEEE.

[106] O'Sullivan, F. et al., (2005). Journal of Applied Physics, 97(3).

[107] St-Gelais, R. et al., (2017). ACS nano, 11(3), 3001-3009.

[108] Gregory, O. J. et al., (2002). Thin Solid Films, 406(1-2), 286-293.

[109] Naik, G. V. et al., (2011). Optical materials express, 1(6), 1090-1099.

[110] Palik, E. D. (Ed.). (1998). (Vol. 3). Academic press.

[111] Chubb, D. (2007). Fundamentals of thermophotovoltaic energy conversion. Elsevier.

[112] Ordal, M. A. et al., (1985). Applied optics, 24(24), 4493-4499.

[113] Wright, A. H. (1991). In Foundations of genetic algorithms (Vol. 1, pp. 205-218). Elsevier.

[114] Baker, L. et al., (2012). Applied Physics Letters, 101(11).

[115] Aaltonen, T. et al., (2003). Chemistry of materials, 15(9), 1924-1928.

[116] Francoeur, M. et al., (2010). Spectral tuning of near-field radiative heat flux between two thin silicon carbide films. Journal of Physics D: Applied Physics, 43(7), 075501.

BIOGRAPHY OF THE AUTHOR

Mehran Habibzadeh was born in Tehran, Iran, in 1997. He earned his Bachelor’s degree in Mechanical Engineering from K. N. Toosi University of Technology of Tehran in 2020. Mehran is a candidate for the Master of Science degree in Mechanical Engineering from the University of Maine in December 2023.